AIMS Mathematics, 10(7): 15841–15866.
DOI: 10.3934/math.2025710
Received: 25 April 2025
Revised: 09 June 2025
Accepted: 25 June 2025
Published: 14 July 2025

http://www.aimspress.com/journal/Math

Research article

Fractional modeling of vector-borne disease dynamics using ABC operators and neural networks

Ateq Alsaadi*

Department of Mathematics and Statistics, College of Science, Taif University, P.O. Box 11099, Taif 21944, Saudi Arabia

* **Correspondence:** Email: ateq@tu.edu.sa.

Abstract: This work enhanced the mathematical modeling of vector-borne infections involving vertical transmission and treatment effects within a targeted population by incorporating fractional calculus techniques that account for nonlocal properties and non-singular fading memory behavior. This work investigated a fractional-order mathematical model for poliomyelitis governed by the Mittag-Leffler kernel. By employing fixed point theory, we qualitatively analyzed the model and confirmd the existence and uniqueness of solutions. Additionally, Ulam's type stability is examined through nonlinear analytical methods. To approximate the solution, a fractional Adams-Bashforth numerical scheme is utilized. The model was simulated under various fractional orders and different control scenarios. Results indicate that all compartments exhibit convergence and long-term stability. Notably, lower fractional orders tend to reach stability more rapidly. Furthermore, Artificial Neural Networks were applied, with the dataset partitioned into training, validation, and testing subsets. A comprehensive assessment was carried out for each dataset partition.

Keywords: Adams-Bashforth method; Mittag-Leffler kernel; fixed point theory; vector-borne diseases
Mathematics Subject Classification: 34D20, 34K20, 34K60, 92C60, 92D45

1. Introduction

Vector-borne illnesses are transmitted through the bites of blood-feeding arthropods and can affect both humans and animals. Examples of these diseases include dengue fever, West Nile virus, malaria, and viral encephalitis, among others [1]. Pathogens, including viruses, bacteria, or parasites, typically trigger these illnesses. Blood-sucking arthropods-such as mosquitoes, ticks, and biting flies-serve as carriers, transmitting these pathogens to new hosts by feeding on infected individuals [2].

Such diseases are particularly prevalent in tropical and sub-Saharan regions, where warm climates

provide ideal conditions for the survival of vectors. They represent a significant portion of global health burdens and are responsible for millions of cases and fatalities annually [3]. According to the World Health Organization, mosquito-borne infections impact nearly 700 million people each year, with an estimated one million deaths reported worldwide [4, 5]. These alarming figures underscore the necessity of effectively monitoring, modeling, and controlling the spread of vector-borne infections [5].

In this regard, mathematical models play a crucial role in analyzing the transmission patterns of diseases such as poliomyelitis. Recent advancements have seen the development of both classical and modern modeling approaches-including those based on ordinary and partial differential equations-to investigate the behavior and spread of poliovirus [6]. The formulation of the current model is given below in the form of a system of differential equations:

$$\begin{aligned}
\frac{dS}{dt} &= (1-\epsilon_1 I)b_1 - \beta_1 S I - \beta_2 S W - \mu_1 S,\\
\frac{dI}{dt} &= \epsilon_1 b_1 I + \beta_1 S I + \beta_2 S W - \alpha I - \eta I - \delta_1 I - \mu_1 I,\\
\frac{dT}{dt} &= \alpha I - \gamma I - \delta_1 T - \mu_1 T,\\
\frac{dR}{dt} &= \eta I + \gamma T - \mu_1 R,\\
\frac{dV}{dt} &= (1-\epsilon_2 W)b_2 + \beta_3 V I - \mu_2 W,\\
\frac{dW}{dt} &= \epsilon_2 b_2 W + \beta_3 V I - \delta_2 W - \mu_2 W.
\end{aligned} \tag{1.1}$$

Fractional calculus has garnered significant interest from the scientific community due to its broad applicability across various scientific and engineering fields. In recent years, numerous disease models incorporating fractional dynamics have been proposed and analyzed [7–9]. While classical models primarily rely on integer-order differential and integral equations, there has been a growing shift toward employing fractional differential equations over the past two decades, as they offer enhanced modeling capabilities with improved accuracy and realism [10].

In [11], Javidi also developed a fractional-order model based on cholera infection. Using Liouville-Caputo fractional derivatives, an autochthonic model with constant population for Okyere has been studied analytically and numerically. In [12], Erturk asked about a quitting smoking model connected to the Caputo fractional derivative. The authors presented a novel smoking model with fractional yielding in [13], based on the Caputo-Fabrizio-Caputo fractional derivative. The actuality and uniqueness of the answer were discussed through the application of the fixed point postulate [14, 15]. A wide array of analytical techniques has been explored to qualitatively examine the behavior of fractional-order systems, as documented in several studies [16, 17]. Nonetheless, the nonlinearity inherent in many FDEs poses significant challenges for obtaining explicit solutions. To overcome these difficulties, researchers have proposed various approximate methods for effectively solving nonlinear fractional systems [18, 19].

To overcome the limitations associated with classical differential operators, several types of fractional-order derivatives have been introduced over time [20]. One of the earliest forms, proposed by Riemann and later refined by Caputo, led to the Caputo fractional derivative-characterized by its reliance on a singular power-law kernel. However, when applied to real-world problems, such

formulations often encounter singularities, which hinder the robustness of mathematical modeling.

To mitigate this issue, the Caputo-Fabrizio derivative was developed, featuring a nonsingular kernel to eliminate singular behavior [21]. Despite this improvement, the CF operator still faced concerns regarding kernel locality. To resolve both singularity and localization issues, Atangana and Baleanu (AB) introduced a new type of fractional derivative incorporating a nonsingular and nonlocal Mittag-Leffler kernel [22]. This operator not only avoids the problems of singularities and localization but also expands the scope of application across various scientific disciplines.

Recently, researchers have focused on the Artificial Neural Networks (ANNs) method and analyzed various types of linear and nonlinear mathematical models [23]. Due to its successful applications in various scientific and engineering domains, including signal processing, image processing, control systems, and associative memory, among others, ANNs have become a viable alternative for simulating complex systems. Furthermore, the memory description is the primary feature of integer-order calculus, which is expanded upon and generalized in fractional calculus. Due to these characteristics, ANN processing enables a wide range of applications, including recognition, prediction, decision-making, classification, region-based traffic flow prediction, image processing, and an image measuring system, among many other fields [24, 25].

2. Model formulation

In this study, we employ the Atangana-Baleanu-Caputo (ABC) fractional derivative due to its ability to capture long-term memory effects in biological systems through a nonsingular and nonlocal Mittag-Leffler kernel. Unlike the Caputo-Fabrizio operator, which employs an exponentially decaying kernel, the ABC operator's Mittag-Leffler function offers a slower decay and a more realistic representation of memory, particularly relevant in the context of infectious diseases, where historical states-such as past infections or treatments-can influence present dynamics. This makes the ABC derivative particularly suitable for modeling chronic or relapsing vector-borne diseases, offering greater flexibility and biological relevance in capturing the temporal evolution of disease compartments. The formulation is constructed using the ABC fractional derivative, and the governing equations are outlined as follows:

$$\begin{aligned}
{}^{\mathbb{ABC}}D_t^{\varphi} S &= (1-\epsilon_1 I)b_1 - \beta_1 S I - \beta_2 S W - \mu_1 S,\\
{}^{\mathbb{ABC}}D_t^{\varphi} I &= \epsilon_1 b_1 I + \beta_1 S I + \beta_2 S W - \alpha I - \eta I - \delta_1 I - \mu_1 I,\\
{}^{\mathbb{ABC}}D_t^{\varphi} T &= \alpha I - \gamma I - \delta_1 T - \mu_1 T,\\
{}^{\mathbb{ABC}}D_t^{\varphi} R &= \eta I + \gamma T - \mu_1 R,\\
{}^{\mathbb{ABC}}D_t^{\varphi} V &= (1-\epsilon_2 W)b_2 + \beta_3 V I - \mu_2 W,\\
{}^{\mathbb{ABC}}D_t^{\varphi} W &= \epsilon_2 b_2 W + \beta_3 V I - \delta_2 W - \mu_2 W,
\end{aligned} \tag{2.1}$$

along with initial conditions

$$\begin{aligned}
&S(0) = S(0) \geq 0,\ I(0) = I(0) \geq 0,\ T(0) = T(0) \geq 0,\ R(0) = R(0) \geq 0,\\
&V(0) = V(0) \geq 0,\ W(0) = W(0) \geq 0.
\end{aligned} \tag{2.2}$$

$S(\mathfrak{I})$, $I(\mathfrak{I})$, $T(\mathfrak{I})$, and $R(\mathfrak{I})$ represent the sizes of the susceptible, infectious, under-treatment, and recovered human populations at time $\mathfrak{I}$, respectively. The vector population is divided into two

compartments: $V(\mathfrak{I})$ for susceptible vectors and $W(\mathfrak{I})$ for infected vectors. The model incorporates various parameters: β_1 denotes the rate of direct human-to-human transmission, while β_2 accounts for the vector-mediated transmission rate. The parameter β_3 represents the rate at which mosquitoes become infected after biting infected humans. The rate at which infectious individuals begin treatment is given by α, and the recovery rate of treated individuals is denoted by γ. The natural recovery rate from the infectious class is represented by η. The birth rates for humans and vectors are given by b_1 and b_2, respectively. Fractions ϵ_1 and ϵ_2 capture the proportion of newborn humans infected at birth from infected parents. Natural death rates for humans and vectors are given by μ_1 and μ_2, while δ_1 and δ_2 represent the disease-induced mortality rates in humans and vectors, respectively.

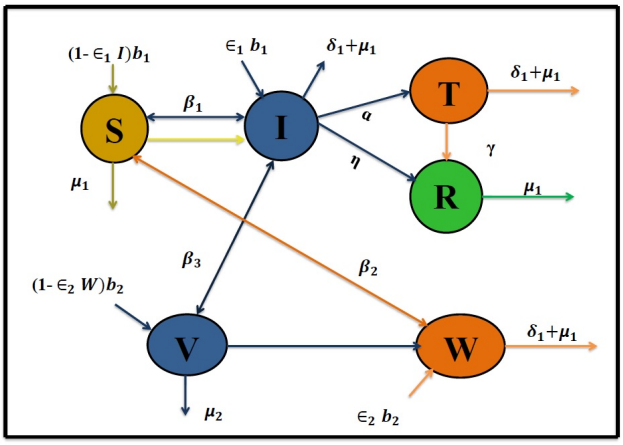

Figure 1. The flow diagram of model 2.1.

3. Preliminaries

This section outlines some essential concepts and preliminary definitions that may assist readers in understanding the subsequent analysis [22]. For simplicity, we use FD and FI to represent the fractional derivative and fractional integral, respectively.

Definition 3.1. *Let* $0 < \iota \leq 1$ *and* $\mathscr{X}(\mathfrak{I}) \in \mathcal{H}^1[0,T]$. *The ABC fractional derivative of order* ι *is defined as*

$$^{\mathbb{ABC}}D^{\iota}_{\mathfrak{I}}(\mathscr{X}(\mathfrak{I})) = \frac{\mathbb{N}(\iota)}{1-\iota}\int_0^{\mathfrak{I}} \mathbf{E}_{\iota}\left(\frac{-\iota}{1-\iota}(\mathfrak{I}-\tau)^{\iota}\right)\frac{d}{d\tau}\mathscr{X}(\tau)\,d\tau, \tag{3.1}$$

where $\mathbb{N}(\iota)$ *is a normalization function satisfying* $\mathbb{N}(0) = \mathbb{N}(1) = 1$, *and* $\mathbf{E}_{\iota}(x)$ *is the one-parameter Mittag-Leffler function expressed as*

$$\mathbf{E}_{\iota}(y) = \sum_{k=0}^{\infty}\frac{x^k}{\Gamma(\iota k+1)},$$

with $\Gamma(\cdot)$ *being the Gamma function and* $Re(\iota) > 0$.

Definition 3.2. *For* $\mathscr{X} \in L^1(0,T)$, *the ABC fractional integral of order* ι *is defined by*

$$^{\mathbb{ABC}}I^{\iota}_{\mathfrak{I}}\mathscr{X}(\mathfrak{I}) = \frac{1-\iota}{\mathbb{N}(\iota)}\mathscr{X}(\mathfrak{I}) + \frac{\iota}{\mathbb{N}(\iota)}\cdot\frac{1}{\Gamma(\wp)}\int_0^{\mathfrak{I}}(\mathfrak{I}-\tau)^{\iota-1}\mathscr{X}(\tau)\,d\tau, \quad \mathfrak{I} > 0. \tag{3.2}$$

Lemma 3.1. *Let us consider*

$$\begin{aligned} {}^{\mathbb{ABC}}D^{\wp}_{\mathfrak{I}}\mathscr{X}(\mathfrak{I}) &= \Psi(\mathfrak{I}), \\ \mathscr{X}(0) &= \mathscr{X}_0, \end{aligned} \tag{3.3}$$

then

$$\mathscr{X}(\mathfrak{I}) = \mathscr{X}_0 + \frac{1-\iota}{\mathbb{N}(\iota)}\Psi(\mathfrak{I}) + \frac{\iota}{\mathbb{N}(\iota)}\frac{1}{\Gamma(\iota)}\int_0^{\mathfrak{I}}(\mathfrak{I}-s)^{\iota-1}\Psi(s)ds. \tag{3.4}$$

Proof. Integrating each side of Eq (3.3), we obtain:

$${}^{\mathbb{ABC}}_{0}\mathbf{I}_{\mathfrak{I}}\Big[{}^{\mathbb{ABC}}D^{\iota}_{\mathfrak{I}}\mathscr{X}(\mathfrak{I})\Big] = {}^{\mathbb{ABC}}_{0}\mathbf{I}_{\mathfrak{I}}\Big[\Psi(\mathfrak{I})\Big],$$

we get as follows

$$\mathscr{X}(\mathfrak{I}-\mathscr{X}(0) = \frac{1-\iota}{\mathbb{N}(\iota)}\Psi(\mathfrak{I}) + \frac{\iota}{\mathbb{N}(\iota)}\frac{1}{\Gamma(\iota)}\int_0^{\mathfrak{I}}(\mathfrak{I}-s)^{(\iota-1)}\Psi(s)ds,$$

or

$$\mathscr{X}(\mathfrak{I}) = \mathscr{X}(0) + \frac{1-\iota}{\mathbb{N}(\iota)}\Psi(\mathfrak{I}) + \frac{\iota}{\mathbb{N}(\iota)}\frac{1}{\Gamma(\iota)}\int_0^{\mathfrak{I}}(\mathfrak{I}-s)^{(\iota-1)}\Psi(s)ds,$$

The proof is thus finalized. □

Theorem 1. *Consider a Banach space O and suppose that $Q \subset$ is a nonempty, closed, bounded, and convex set. Let $\psi : \mathtt{Q} \to \mathtt{Q}$ be a continuous mapping. If $\psi(\mathtt{D}) \subset O$ and $\psi(\mathtt{D})$ is relatively compact, then the operator ψ admits at least one fixed point in $\mathtt{D}$.*

4. Qualitative study of model (2.1)

4.1. Existence theory

By employing well-established results from fixed point theory, we investigate the existence, uniqueness, and stability of the solution for the model given in Eq (2.1). To facilitate this analysis, we reformulate the model accordingly to derive the desired results:

$$\begin{cases} {}^{\mathbb{ABC}}D^{\iota}_{\mathfrak{I}}S(\mathfrak{I}) = \mathbb{G}_1(\mathfrak{I},S,I,T,R,V,W), \\ {}^{\mathbb{ABC}}D^{\iota}_{\mathfrak{I}}I(\mathfrak{I}) = \mathbb{G}_2(\mathfrak{I},S,I,T,R,V,W), \\ {}^{\mathbb{ABC}}D^{\iota}_{\mathfrak{I}}T(\mathfrak{I}) = \mathbb{G}_3(\mathfrak{I},S,I,T,R,V,W), \\ {}^{\mathbb{ABC}}D^{\iota}_{\mathfrak{I}}R(\mathfrak{I}) = \mathbb{G}_4(\mathfrak{I},S,I,T,R,V,W), \\ {}^{\mathbb{ABC}}D^{\iota}_{\mathfrak{I}}V(\mathfrak{I}) = \mathbb{G}_5(\mathfrak{I},S,I,T,R,V,W), \\ {}^{\mathbb{ABC}}D^{\iota}_{\mathfrak{I}}W(\mathfrak{I}) = \mathbb{G}_6(\mathfrak{I},S,I,T,R,V,W), \end{cases} \tag{4.1}$$

where

$$\begin{cases} \mathbb{G}_1(\mathfrak{I}, S, I, T, R, V, W) = (1-\epsilon_1 I)b_1 - \beta_1 S I - \beta_2 S W - \mu_1 S, \\ \mathbb{G}_2(\mathfrak{I}, S, I, T, R, V, W) = \epsilon_1 b_1 I + \beta_1 S I + \beta_2 S W - \alpha I - \eta I - \delta_1 I - \mu_1 I, \\ \mathbb{G}_3(\mathfrak{I}, S, I, T, R, V, W) = \alpha I - \gamma I - \delta_1 T - \mu_1 T, \\ \mathbb{G}_4(\mathfrak{I}, S, I, T, R, V, W) = \eta I + \gamma T - \mu_1 R, \\ \mathbb{G}_5(\mathfrak{I}, S, I, T, R, V, W) = (1-\epsilon_2 W)b_2 + \beta_3 V I - \mu_2 W, \\ \mathbb{G}_6(\mathfrak{I}, S, I, T, R, V, W) = \epsilon_2 b_2 W + \beta_3 V I - \delta_2 W - \mu_2 W. \end{cases} \tag{4.2}$$

Next, we express the models (2.1) and (2.2) as

$$\begin{aligned} {}^{\mathbb{ABC}}D^{\iota}_{\mathfrak{I}}\Psi(\mathfrak{I}) &= \Omega(\mathfrak{I}, \Psi(\mathfrak{I})), \\ \Psi(0) &= \Psi_0, \end{aligned} \tag{4.3}$$

where

$$\begin{cases} \Psi := (S, I, T, R, V, W)^T, \\ \Psi(0) := (S(0), I(0), T(0), R(0), V(0), W(0))^T, \\ \Omega(\mathfrak{I}, \Psi(\mathfrak{I})) := \mathbb{G}_i(\mathfrak{I}, S, I, T, R, V, W)^T, \quad i = 1, 2, 3, 4, 5, 6. \end{cases} \tag{4.4}$$

It is worth noting that $(\cdot)^T$ denotes the transpose of a vector. By applying Lemma 3.1, the system in Eq (4.3) is reformulated as follows:

$$\Psi(\mathfrak{I}) = \Psi_0 + \frac{1-\iota}{\mathbb{N}(\iota)}\Omega(\mathfrak{I}, \Psi(\mathfrak{I})) + \frac{\iota}{\mathbb{N}(\iota)\Gamma(\iota)}\int_0^{\mathfrak{I}} (\mathfrak{I}-s)^{\iota-1}\Omega(s, \Psi(s))ds. \tag{4.5}$$

Let

$$\Upsilon = C([0, T], \mathbb{R})$$

be the space of continuous real-valued functions on the interval $[0, T]$. We define the Banach space

$$\mathbb{Z} = (\Upsilon^6, \|\Psi\|),$$

where the norm is given by

$$\|\Psi\| = \sup_{\mathfrak{I}\in[0,T]} \left(|S(\mathfrak{I})| + |I(\mathfrak{I})| + |T(\mathfrak{I})| + |R(\mathfrak{I})| + |V(\mathfrak{I})| + |W(\mathfrak{I})|\right).$$

In the following, we investigate the existence of solutions for the proposed systems (2.1) and (2.2) using Schauder's fixed point theorem.

Theorem 2. *Suppose $\Omega \in \mathbb{Z}$ is a continuous function, and there exists a constant $\mathcal{M} > 0$ such that*

$$|\Omega(\mathfrak{I}, \Psi(\mathfrak{I}))| \leq \mathcal{M}(1 + |\Psi|), \quad \forall \mathfrak{I} \in [0, T],\ \Psi \in \mathbb{Z}.$$

If the following condition holds:

$$\nabla_1 = \left(\frac{(1-\jmath)\Gamma(\iota)\mathcal{M} + \mathcal{M}T^{\iota}}{\mathbb{N}(\iota)\Gamma(\iota)}\right) < 1,$$

then it follows that the model possesses at least one solution.

Proof. We define $\mathbf{Y} : F \to F$ as

$$(\mathbf{Y}\Psi)(\mathfrak{I}) = \Psi_0 + \frac{1-\iota}{\mathbb{N}(\iota)}\Omega(\mathfrak{I}, \Psi(\mathfrak{I})) + \frac{\iota}{\mathbb{N}(\iota)\Gamma(\iota)}\int_0^{\mathfrak{I}} (\mathfrak{I}-s)^{\wp-1}\Omega(s, \Psi(s))ds. \tag{4.6}$$

Define

$$\mathtt{B}_{\varpi} = \{\Psi \in \Omega : \|\Psi\| \leq \varpi,\ \varpi > 0\}$$

to be a closed and convex ball, where

$$\varpi \geq \frac{\nabla_2}{1-\nabla_1},$$

$$\nabla_2 = |\Psi_0| + \frac{1-\iota}{\mathbb{N}(\iota)}\mathcal{M} + \frac{T^{\iota}}{\mathbb{N}(\iota)\Gamma(\iota)}\mathcal{M}. \tag{4.7}$$

To begin, it is necessary to establish that $\mathbf{Y}(\mathtt{B}_{\varpi}) \subset \mathtt{B}_{\varpi}$ for all $\mathfrak{I} \in [0, T]$. It can be shown that:

$$\begin{aligned} |(\mathbf{Y}\Psi)(\mathfrak{I})| &\leq |\Psi_0| + \frac{1-\iota}{\mathbb{N}(\iota)}|\Omega(\mathfrak{I}, \Psi(\mathfrak{I}))| + \frac{\iota}{\mathbb{N}(\iota)\Gamma(\iota)}\int_0^{\mathfrak{I}} (\mathfrak{I}-s)^{\wp-1}|\Omega(s, \Psi(s))|ds, \\ &\leq |\Psi_0| + \frac{1-\iota}{\mathbb{N}(\iota)}\mathbb{N}(1+|\Psi(\mathfrak{I})|) + \frac{\iota}{\mathbb{N}(\iota)\Gamma(\iota)}\int_0^{\mathfrak{I}} (\mathfrak{I}-s)^{\iota-1}\mathbb{N}(1+|\Psi(\mathfrak{I})|)ds. \end{aligned} \tag{4.8}$$

Since $\Psi \in \mathtt{B}_{\varpi}$, it follows that we can express:

$$\begin{aligned} \|(\mathbf{Y}\Psi)(\mathfrak{I})\| &\leq |\Psi_0| + \frac{1-\iota}{\mathbb{N}(\iota)}\mathcal{M}(1+\|\Psi(\mathfrak{I})\|) + \frac{T^{\iota}}{\mathbb{N}(\iota)\Gamma(\iota)}\mathcal{M}(1+\|\Psi(\mathfrak{I})\|), \\ &\leq |\Psi_0| + \frac{1-\iota}{\mathbb{N}(\iota)}\mathcal{M} + \frac{T^{\iota}}{\mathbb{N}(\iota)\Gamma(\iota)}\mathcal{M} + \left[\frac{1-\iota}{\mathbb{N}(\iota)}\mathcal{M} + \frac{T^{\iota}}{\mathbb{N}(\iota)\Gamma(\iota)}\mathcal{M}\right]\rho, \\ &\leq \nabla_2 + \nabla_1\varpi \leq \varpi. \end{aligned}$$

Therefore, we have $\mathbf{Y}(\mathtt{B}_{\varpi}) \subset \mathtt{B}_{\varpi}$. The next step is to confirm the continuity of the operator $\mathbf{Y}$. Consider a sequence $\{\Psi_n\}$ in $\mathtt{B}_{\varpi}$ such that $\Psi_n \to \Psi$ as $n \to \infty$. Then, it follows that:

$$\begin{aligned} \left|(\mathbf{Y}\Psi_n)(\mathfrak{I}) - (\mathbf{Y}\Psi)(\mathfrak{I})\right| &\leq \frac{-\iota+1}{\mathbb{N}(\iota)}\left|\Omega(\mathfrak{I}, \Psi_n(\mathfrak{I})) - \Omega(\mathfrak{I}, \Psi(\mathfrak{I}))\right| + \frac{\iota}{\mathbb{N}(\iota)\Gamma(\iota)} \\ &\quad \times \int_0^{\mathfrak{I}} (\mathfrak{I}-s)^{\iota-1}\left|\Omega(s, \Psi_n(s)) - \Omega(s, \Psi(s))\right|ds \\ &\leq \frac{1-\iota}{\mathbb{N}(\iota)}\|\Omega(\mathfrak{I}, \Psi_n(\mathfrak{I})) - \Omega(\mathfrak{I}, \Psi(\mathfrak{I}))\| \\ &\quad + \frac{T^{\iota}}{\mathbb{N}(\iota)\Gamma(\iota)}\|\Omega(s, \Psi_n(s)) - \Omega(s, \Psi(s))\|. \end{aligned}$$

It follows that

$$\|(\mathbf{Y}\Psi_n) - (\mathbf{Y}\Psi)\| \to 0 \quad \text{as} \quad n \to \infty.$$

The continuity of $\mathbf{Y}$ on $\mathtt{B}_{\varpi}$ has been established. Next, we aim to demonstrate that $\mathbf{Y}(\mathtt{B}_{\varpi})$ is relatively compact. Since it has already been shown that $\mathbf{Y}(\mathtt{B}_{\varpi}) \subset \mathtt{B}_{\varpi}$, it follows that the image is uniformly bounded. We now proceed to verify the equi-continuity of the operator $\mathbf{Y}$ on $\mathtt{B}_{\varpi}$. Let $\Psi \in \mathtt{B}_{\varpi}$ and $\mathfrak{I}_1, \mathfrak{I}_2 \in [0, T]$ with $\mathfrak{I}_1 < \mathfrak{I}_2$. Then, we obtain:

$$\begin{aligned}
\|(\mathbf{Y}\Psi)(\mathfrak{I}_2) - (\mathbf{Y}\Psi)(\mathfrak{I}_1)\| &\leq \frac{1-\iota}{\mathbb{N}(\iota)}\Big|\Omega(\mathfrak{I}_2, \Psi(\mathfrak{I}_2)) - \Omega(\mathfrak{I}_1, \Psi(\mathfrak{I}_1))\Big| \\
&+ \frac{\iota}{\mathbb{N}(\iota)\Gamma(\iota)}\Big|\Big[\int_0^{\mathfrak{I}_2}(\mathfrak{I}_2 - s)^{\iota-1} - \int_0^{\mathfrak{I}_1}(\mathfrak{I}_1 - s)^{\iota-1}\Big]\Omega(s, \Psi(s))ds\Big| \\
&\leq \frac{1-\iota}{\mathbb{N}(\iota)}\Big|\Omega(\mathfrak{I}_2, \Psi(\mathfrak{I}_2)) - \Omega(\mathfrak{I}_1, \Psi(\mathfrak{I}_1))\Big| \\
&+ \frac{\iota}{\mathbb{N}(\iota)}\frac{\mathcal{M}(1 + \|\Psi\|)}{\Gamma(\iota+1)}(\mathfrak{I}_2^{\iota} - \mathfrak{I}_1^{\iota}).
\end{aligned}$$

It is evident that

$$\|\mathbf{Y}\Psi(\mathfrak{I}_2) - \mathbf{Y}\Psi(\mathfrak{I}_1)\| \to 0$$

as $\mathfrak{I}_2 \to \mathfrak{I}_1$. According to the Arzelà-Ascoli theorem, the operator $(\mathbf{Y}\mathtt{B}_{\varpi})$ is relatively compact, which implies that $\mathbf{Y}$ is completely continuous. Hence, by Theorem 1, the operator admits at least one fixed point. Therefore, the proposed fractional-order model possesses at least one solution. □

Theorem 3. *If all the functions $G_i \in C(J, \mathbb{R})$ are Lipschitz continuous with Lipschitz constants L_i, then the system (4.5) has a unique solution.*

Proof. To rigorously validate the applicability of 2, we verify that each nonlinear function G_i in the model satisfies the Lipschitz condition. Each G_i corresponds to the right-hand side of a compartmental differential equation and depends on biologically bounded variables such as $S(\mathfrak{I})$, $I(\mathfrak{I})$, $T(\mathfrak{I})$, $R(\mathfrak{I})$, $V(\mathfrak{I})$, and $W(\mathfrak{I})$. Given that total population sizes are constrained by natural limits and all state variables remain non-negative and bounded over time, we can define constants L_i such that

$$|G_i(x) - G_i(y)| \leq L_i|x - y|$$

for all $x, y \in \mathbb{R}^n$. Furthermore, the perturbation function $\Omega_{\mathfrak{I}}$ and the auxiliary function ψ are assumed to satisfy $\Omega_{\mathfrak{I}}, \psi \leq M_1 + \psi$, where M_1 is a bound derived from initial conditions and system parameters. This boundedness, justified by biological feasibility, guarantees that all necessary conditions for applying the Banach fixed-point theorem are met, thereby establishing the uniqueness of the solution. □

4.2. Stability result

In this section, we examine the Ulam-type stability of the model (2.1) using Ulam-Hyers methodology. This is achieved by introducing a perturbation function $\Omega(\mathfrak{I})$, which primarily depends on the system's solution, subject to the initial condition $\Omega(0) = 0$, as described below:

- $|\Omega(\mathfrak{I})| \leq \epsilon$ for $\epsilon > 0$;
- ${}_0^{\mathbb{ABC}}\mathbf{D}_{\mathfrak{I}}^{\iota}\Psi(\mathfrak{I}) = y(\mathfrak{I}, \Psi) + \Omega(\mathfrak{I})$.

Lemma 4.1. *The solution of*

$$\begin{aligned} {}^{\mathbb{ABC}}_{0}\mathbf{D}^{\iota}_{\mathfrak{I}}\Psi(\mathfrak{I}) &= y(\mathfrak{I},\Psi(\mathfrak{I}))+\Omega(\mathfrak{I}),\ 0<\iota\leq 1 \quad \mathfrak{I}\in[0,T], \\ \Psi(0) &= \Psi_0, \end{aligned} \tag{4.9}$$

satisfies

$$\begin{aligned} &\left|\Psi(\mathfrak{I})-\left(\Psi_0(\mathfrak{I})+[y(\mathfrak{I},\Psi(\mathfrak{I}))+\Omega(\mathfrak{I})]\frac{(1-\iota)}{\mathbb{N}(\iota)}+\frac{\iota}{\mathbb{N}(\iota)\Gamma(\iota)}\int_0^{\mathfrak{I}}(\mathfrak{I}-s)^{\iota-1}[y(s,\Psi(s))+\Omega(s)]ds\right)\right|, \\ &\leq \frac{(1-\iota)\Gamma(\iota+1)+\iota T^{\iota}}{\mathbb{N}(\iota)\Gamma(\wp+1)}\epsilon \\ &= \Lambda\epsilon, \end{aligned} \tag{4.10}$$

where

$$\Lambda=\frac{(1-\iota)\Gamma(\iota+1)+\iota T^{\iota}}{\mathbb{N}(\iota)\Gamma(\iota+1)}.$$

Theorem 4. *Assume* $\Omega\in F$ *and*

$$\exists\mathbf{X}>0\ni\left|\Omega(\mathfrak{I},\Psi)-\Omega(\mathfrak{I},\widetilde{\Psi})\right|\leq\mathbf{X}\left|\Psi-\widetilde{\Psi}\right|,\forall\ \ \mathfrak{I}\in[0,T]$$

and $\Psi\in F$ *with*

$$1>\frac{(1-\iota)\Gamma(\iota+1)\mathbf{X}+\iota T^{\iota}}{\mathbb{N}(\iota)\Gamma(\iota+1)}.$$

Assume that Ψ *and* $\widetilde{\Psi}$ *are two solutions corresponding to the system* (4.3)*, and*

$$\begin{cases} {}^{\mathbb{ABC}}\mathrm{D}^{\iota}\widetilde{\Psi}(\mathfrak{I})=\Omega(\mathfrak{I},\widetilde{\Psi}(\mathfrak{I})), \\ \widetilde{\Psi}(0)=\Psi_0+\epsilon\geq 0, \end{cases} \tag{4.11}$$

where

$$\begin{cases} \widetilde{\Psi}=(\widetilde{S},\widetilde{I},\widetilde{T},\widetilde{R},\widetilde{V},\widetilde{W})^{T} \\ \Psi_0+\epsilon=\left(S(0)+\varepsilon+I(0)+\varepsilon,T(0)+\varepsilon,R(0)+\varepsilon,V(0)+\varepsilon,W(0)+\varepsilon\right)^{T} \\ \Omega(\mathfrak{I},\widetilde{\Psi}(\mathfrak{I}))=\mathbb{G}_i(\widetilde{S},\widetilde{I},\widetilde{T},\widetilde{R},\widetilde{V},\widetilde{W})^{T},\ \ i=1,2,3,4,5,6. \end{cases} \tag{4.12}$$

Then,

$$\|\Psi-\widetilde{\Psi}\|\leq\left[1-\frac{(1-\iota)\Gamma(\iota+1)\mathbf{X}+\iota T^{\iota}}{\mathbb{N}(\iota)\Gamma(\iota+1)}\right]^{-1}|\varepsilon|. \tag{4.13}$$

Proof. As the reformulated version of system (4.11) takes the form:

$$\begin{aligned} \widetilde{\Psi}(\mathfrak{I}) &= \Psi_0+\epsilon+\frac{1-\iota}{\mathbb{N}(\iota)}\Omega(\mathfrak{I},\widetilde{\Psi}(\mathfrak{I})) \\ &\quad+\frac{\iota}{\mathbb{N}(\iota)\Gamma(\iota)}\int_0^{\mathfrak{I}}(\mathfrak{I}-s)^{\iota-1}\Omega(s,\widetilde{\Psi}(s))ds. \end{aligned} \tag{4.14}$$

Now, $\forall\ \mathfrak{I} \in [0, T]$, consider

$$\begin{aligned}
|\Psi(\mathfrak{I}) - \widetilde{\Psi}(\mathfrak{I})| &\leq |\varepsilon| + \frac{1-J}{\mathbb{N}(\iota)}\Big|\Omega(\mathfrak{I}, \Psi(\mathfrak{I})) - \Omega(\mathfrak{I}, \widetilde{\Psi}(\mathfrak{I}))\Big| + \frac{\iota}{\mathbb{N}(\iota)\Gamma(\iota)} \\
&\times \int_0^{\mathfrak{I}} (\mathfrak{I} - s)^{\iota-1}\Big|\Omega(s, \Psi(s)) - \Omega(s, \widetilde{\Psi}(s))\Big| ds, \\
&\leq |\varepsilon| + \frac{1-\iota}{\mathbb{N}(\iota)} X\Big|\Psi(\mathfrak{I}) - \widetilde{\Psi}(\mathfrak{I})\Big| + \frac{\iota}{\mathbb{N}(\iota)\Gamma(\iota)} \\
&\times \int_0^{\mathfrak{I}} (\mathfrak{I} - s)^{\iota-1}\mathbf{X}\Big|\Psi(s) - \widetilde{\Psi}(s)\Big| ds, \\
&\leq |\varepsilon| + \left[\frac{1-\iota}{\mathbb{N}(\iota)} + \frac{\iota T^{\wp}}{\mathbb{N}(\iota)\Gamma(\iota+1)}\right]\mathbf{X}\|\Psi - \widetilde{\Psi}\|.
\end{aligned}$$

We have

$$\|\Psi - \widetilde{\Psi}\| \leq |\varepsilon| + \left[\frac{(1-\iota)\Gamma(\iota) + \iota T^{\iota}}{\mathbb{N}(\iota)\Gamma(\iota+1)}\right] G\|\Psi - \widetilde{\Psi}\|.$$

Hence

$$\|\Psi - \widetilde{\Psi}\| \leq \left[1 - \frac{(1-\iota)\Gamma(\iota+1)\mathbf{X} + \iota T^{\iota}}{\mathbb{N}(\iota)\Gamma(\iota+1)}\right]^{-1} |\varepsilon|. \tag{4.15}$$

Thus, the proof is complete. □

The concept of Ulam-Hyers stability plays a vital role in the epidemiological interpretation of the model. It ensures that the solutions of the system remain close to approximate solutions under small perturbations in initial conditions or parameters. This stability property reflects the robustness of the model in the presence of data uncertainty, modeling errors, or real-world disturbances such as slight variations in intervention strategies or reporting inconsistencies. In practical terms, this implies that small errors in parameter estimation or initial disease data will not lead to significant deviations in model predictions, thereby reinforcing the model's reliability and resilience in guiding public health decision-making.

5. Numerical scheme

This section is devoted to the numerical investigation of the systems (2.1) and (2.2). The computations are performed using the developed numerical technique. To facilitate this, the model is rewritten using the FI formulation as follows:

$$\begin{cases} S(\mathfrak{I}) - S(0) = {}^{\mathbb{ABC}}\mathbb{I}_0^{\wp}\mathbb{K}_1(\mathfrak{I}, S(\mathfrak{I})), \\ I(\mathfrak{I}) - I(0) = {}^{\mathbb{ABC}}\mathbb{I}_0^{\wp}\mathbb{K}_2(\mathfrak{I}, I(\mathfrak{I})), \\ T(\mathfrak{I}) - T(0) = {}^{\mathbb{ABC}}\mathbb{I}_0^{\wp}\mathbb{K}_3(\mathfrak{I}, T(\mathfrak{I})), \\ R(\mathfrak{I}) - R(0) = {}^{\mathbb{ABC}}\mathbb{I}_0^{\wp}\mathbb{K}_4(\mathfrak{I}, R(\mathfrak{I})), \\ V(\mathfrak{I}) - V(0) = {}^{\mathbb{ABC}}\mathbb{I}_0^{\wp}\mathbb{K}_5(\mathfrak{I}, V(\mathfrak{I})), \\ W(\mathfrak{I}) - W(0) = {}^{\mathbb{ABC}}\mathbb{I}_0^{\wp}\mathbb{K}_6(\mathfrak{I}, W(\mathfrak{I})). \end{cases} \tag{5.1}$$

We have

$$\begin{aligned} S(\mathfrak{I}) - S(0) &= \frac{1-\iota}{\mathbb{N}(\iota)}\mathbb{K}_1(S(\mathfrak{I}), \mathfrak{I}) + \frac{\wp}{\Gamma(\iota)\mathbb{N}(\iota)}\int_0^{\mathfrak{I}}(\mathfrak{I}-s)^{\iota-1}\mathbb{K}_1(S(s), s)ds, \\ I(\mathfrak{I}) - I(0) &= \frac{1-\iota}{\mathbb{N}(\iota)}\mathbb{K}_2(I(\mathfrak{I}), \mathfrak{I}) + \frac{\wp}{\Gamma(\iota)\mathbb{N}(\iota)}\int_0^{\mathfrak{I}}(\mathfrak{I}-s)^{\iota-1}\mathbb{K}_2(I(s), s)ds, \\ T(\mathfrak{I}) - T(0) &= \frac{1-\iota}{\mathbb{N}(\iota)}\mathbb{K}_3(T(\mathfrak{I}), \mathfrak{I}) + \frac{\wp}{\Gamma(\iota)\mathbb{N}(\iota)}\int_0^{\mathfrak{I}}(\mathfrak{I}-s)^{\iota-1}\mathbb{K}_3(T(s), s)ds, \\ R(\mathfrak{I}) - R(0) &= \frac{1-\iota}{\mathbb{N}(\iota)}\mathbb{K}_4(R(\mathfrak{I}), \mathfrak{I}) + \frac{\wp}{\Gamma(\iota)\mathbb{N}(\iota)}\int_0^{\mathfrak{I}}(\mathfrak{I}-s)^{\iota-1}\mathbb{K}_4(R(s), s)ds, \\ V(\mathfrak{I}) - V(0) &= \frac{1-\iota}{\mathbb{N}(\iota)}\mathbb{K}_5(V(\mathfrak{I}), \mathfrak{I}) + \frac{\wp}{\Gamma(\iota)\mathbb{N}(\iota)}\int_0^{\mathfrak{I}}(\mathfrak{I}-s)^{\iota-1}(\mathbb{K}_5(V(s), s)ds, \\ W(\mathfrak{I}) - W(0) &= \frac{1-\iota}{\mathbb{N}(\iota)}\mathbb{K}_6(W(\mathfrak{I}), \mathfrak{I}) + \frac{\wp}{\Gamma(\iota)\mathbb{N}(\iota)}\int_0^{\mathfrak{I}}(\mathfrak{I}-s)^{\iota-1}\mathbb{K}_6(W(s), s)ds. \end{aligned} \tag{5.2}$$

For numerical computations, substituting $\mathfrak{I} = \mathfrak{I}_{\iota+1}$ for $\iota = 0, 1, 2, ...$, into system (5.2) yields:

$$\begin{aligned} S(\mathfrak{I}_{\iota+1}) - S(0) &= \frac{1-\iota}{\mathbb{N}(\iota)}\mathbb{K}_1(S(\mathfrak{I}_\iota), \mathfrak{I}_\iota) + \frac{\iota}{\mathbb{N}(\iota)\Gamma(\iota)}\sum_{\kappa=0}^{\iota}\int_{\mathfrak{I}_\kappa}^{\mathfrak{I}_\kappa+1}(\mathfrak{I}_{\iota+1}-s)^{\iota-1}\mathbb{K}_1(S(s), s)ds, \\ I(\mathfrak{I}_{\iota+1}) - I(0) &= \frac{1-\iota}{\mathbb{N}(\iota)}\mathbb{K}_2(I(\mathfrak{I}_\iota), \mathfrak{I}_\iota) + \frac{\iota}{\mathbb{N}(\iota)\Gamma(\iota)}\sum_{\kappa=0}^{\iota}\int_{\mathfrak{I}_\kappa}^{\mathfrak{I}_\kappa+1}(\mathfrak{I}_{\iota+1}-s)^{\iota-1}\mathbb{K}_2(I(s), s)ds, \\ T(\mathfrak{I}_{\iota+1}) - T(0) &= \frac{1-\iota}{\mathbb{N}(\iota)}\mathbb{K}_3(T(\mathfrak{I}_\iota), \mathfrak{I}_\iota) + \frac{\iota}{\mathbb{N}(\iota)\Gamma(\iota)}\sum_{\kappa=0}^{\iota}\int_{\mathfrak{I}_\kappa}^{\mathfrak{I}_\kappa+1}(\mathfrak{I}_{\iota+1}-s)^{\iota-1}\mathbb{K}_3(T(s), s)ds, \\ R(\mathfrak{I}_{\iota+1}) - R(0) &= \frac{1-\iota}{\mathbb{N}(\iota)}\mathbb{K}_4(R(\mathfrak{I}_\iota), \mathfrak{I}_\iota) + \frac{\iota}{\mathbb{N}(\iota)\Gamma(\iota)}\sum_{\kappa=0}^{\iota}\int_{\mathfrak{I}_\kappa}^{\mathfrak{I}_\kappa+1}(\mathfrak{I}_{\iota+1}-s)^{\iota-1}\mathbb{K}_4(R(s), s)ds, \\ V(\mathfrak{I}_{\iota+1}) - V(0) &= \frac{1-\iota}{\mathbb{N}(\iota)}\mathbb{K}_5(V(\mathfrak{I}_\iota), \mathfrak{I}_\iota) + \frac{\iota}{\mathbb{N}(\iota)\Gamma(\iota)}\sum_{\kappa=0}^{\iota}\int_{\mathfrak{I}_\kappa}^{\mathfrak{I}_\kappa+1}(\mathfrak{I}_{\iota+1}-s)^{\iota-1}\mathbb{K}_5(V(s), s)ds, \\ W(\mathfrak{I}_{\iota+1}) - W(0) &= \frac{1-\iota}{\mathbb{N}(\iota)}\mathbb{K}_6(W(\mathfrak{I}_\iota), \mathfrak{I}_\iota) + \frac{\iota}{\mathbb{N}(\iota)\Gamma(\iota)}\sum_{\kappa=0}^{\iota}\int_{\mathfrak{I}_\kappa}^{\mathfrak{I}_\kappa+1}(\mathfrak{I}_{\iota+1}-s)^{\iota-1}\mathbb{K}_6(W(s), s)ds. \end{aligned} \tag{5.3}$$

Now approximate the functions $\mathbb{K}_1(S(s), s)$, $\mathbb{K}_2(V(s), s)$, $\mathbb{K}_3(E(s), s)$, $\mathbb{K}_4(N_p(s), s)$, $\mathbb{K}_5(P(s), s)$ and $\mathbb{K}_6(A(s), s)$ on the interval $[\mathfrak{I}_\kappa, \mathfrak{I}_{\kappa+1}]$ by using two points interpolation, we have

$$\begin{cases} \mathbb{K}_1(S(s), s) \cong \dfrac{\mathbb{K}_1(S(\Im_\kappa), \Im_\kappa)}{\hbar}(\Im - \Im_{\kappa-1}) + \dfrac{\mathbb{K}_1(S(\Im_{\kappa-1}), \Im_{\kappa-1})}{\hbar}(\Im - \Im_\kappa), \\ \mathbb{K}_2(I(s), s) \cong \dfrac{\mathbb{K}_2(T(\Im_\kappa), \Im_\kappa)}{\hbar}(\Im - \Im_{\kappa-1}) + \dfrac{\mathbb{K}_2(T(\Im_{\kappa-1}), \Im_{\kappa-1})}{\hbar}(\Im - \Im_\kappa), \\ \mathbb{K}_3(T(s), s) \cong \dfrac{\mathbb{K}_3(I(\Im_\kappa), \Im_\kappa)}{\hbar}(\Im - \Im_{\kappa-1}) + \dfrac{\mathbb{K}_3(I(\Im_{\kappa-1}), \Im_{\kappa-1})}{\hbar}(\Im - \Im_\kappa), \\ \mathbb{K}_4(R(s), s) \cong \dfrac{\mathbb{K}_4(R(\Im_\kappa), \Im_\kappa)}{\hbar}(\Im - \Im_{\kappa-1}) + \dfrac{\mathbb{K}_4(R(\Im_{\kappa-1}), \Im_{\kappa-1})}{\hbar}(\Im - \Im_\kappa), \\ \mathbb{K}_5(V(s), s) \cong \dfrac{\mathbb{K}_5(V(\Im_\kappa), \Im_\kappa)}{\hbar}(\Im - \Im_{\kappa-1}) + \dfrac{\mathbb{K}_5(V(\Im_{\kappa-1}), \Im_{\kappa-1})}{\hbar}(\Im - \Im_\kappa), \\ \mathbb{K}_6(W(s), s) \cong \dfrac{\mathbb{K}_6(W(\Im_\kappa), \Im_\kappa)}{\hbar}(\Im - \Im_{\kappa-1}) + \dfrac{\mathbb{K}_6(W(\Im_{\kappa-1}), \Im_{\kappa-1})}{\hbar}(\Im - \Im_\kappa). \end{cases} \tag{5.4}$$

We get

$$\begin{aligned} S(\Im_{\jmath+1}) &= S(0) + \frac{1-\iota}{\mathbb{N}(\iota)}\mathbb{K}_1(S(\Im_\jmath), \Im_\jmath) + \frac{\iota}{\mathbb{N}(\iota)\Gamma(\iota)}\sum_{\kappa=0}^{g}\Big(\frac{\mathbb{K}_1(S(\Im_\kappa), \Im_\kappa)}{\hbar}I_{\kappa-1,\iota} \\ &\quad + \frac{\mathbb{K}_1(S(\Im_{\kappa-1}), \Im_{\kappa-1})}{\hbar}I_{\kappa,\iota}\Big), \\ I(\Im_{\jmath+1}) &= I(0) + \frac{1-\iota}{\mathbb{N}(\iota)}\mathbb{K}_2(I(\Im_\jmath), \Im_\jmath) + \frac{\iota}{\mathbb{N}(\iota)\Gamma(\iota)}\sum_{\kappa=0}^{g}\Big(\frac{\mathbb{K}_2(I(\Im_\kappa), \Im_\kappa)}{\hbar}I_{\kappa-1,\iota} \\ &\quad + \frac{\mathbb{K}_2(I(\Im_{\kappa-1}), \Im_{\kappa-1})}{\hbar}I_{\kappa,\iota}\Big), \\ T(\Im_{\jmath+1}) &= T(0) + \frac{1-\iota}{\mathbb{N}(\iota)}\mathbb{K}_3(T(\Im_\jmath), \Im_\jmath) + \frac{\iota}{\mathbb{N}(\iota)\Gamma(\iota)}\sum_{\kappa=0}^{g}\Big(\frac{\mathbb{K}_3(T(\Im_\kappa), \Im_\kappa)}{\hbar}I_{\kappa-1,\iota} \\ &\quad + \frac{\mathbb{K}_3(T(\Im_{\kappa-1}), \Im_{\kappa-1})}{\hbar}I_{\kappa,\iota}\Big), \\ R(\Im_{\jmath+1}) &= R(0) + \frac{1-\iota}{\mathbb{N}(\iota)}\mathbb{K}_4(R(\Im_\jmath), \Im_\jmath) + \frac{\iota}{\mathbb{N}(\iota)\Gamma(\iota)}\sum_{\kappa=0}^{g}\Big(\frac{\mathbb{K}_4(R(\Im_\kappa), \Im_\kappa)}{\hbar}I_{\kappa-1,\iota} \\ &\quad + \frac{\mathbb{K}_4(R(\Im_{\kappa-1}), \Im_{\kappa-1})}{\hbar}I_{\kappa,\iota}\Big), \\ V(\Im_{\jmath+1}) &= V(0) + \frac{1-\iota}{\mathbb{N}(\iota)}\mathbb{K}_5(V(\Im_\jmath), \Im_\jmath) + \frac{\iota}{\mathbb{N}(\iota)\Gamma(\iota)}\sum_{\kappa=0}^{g}\Big(\frac{\mathbb{K}_5(V(\Im_\kappa), \Im_\kappa)}{\hbar}I_{\kappa-1,\iota} \\ &\quad + \frac{\mathbb{K}_5(V(\Im_{\kappa-1}), \Im_{\kappa-1})}{\hbar}I_{\kappa,\iota}\Big), \\ W(\Im_{\jmath+1}) &= W(0) + \frac{1-\iota}{\mathbb{N}(\iota)}\mathbb{K}_6(W(\Im_\jmath), \Im_\jmath) + \frac{\iota}{\mathbb{N}(\iota)\Gamma(\iota)}\sum_{\kappa=0}^{g}\Big(\frac{\mathbb{K}_6(W(\Im_\kappa), \Im_\kappa)}{\hbar}I_{\kappa-1,\iota} \\ &\quad + \frac{\mathbb{K}_6(W(\Im_{\kappa-1}), \Im_{\kappa-1})}{\hbar}I_{\kappa,\iota}\Big), \end{aligned} \tag{5.5}$$

where

$$I_{\kappa-1,\iota} = \int_{\Im_\kappa}^{\Im_{\kappa+1}} (\Im - \Im_{\kappa-1})(\Im_{\jmath+1} - \Im)^{\iota-1} d\Im$$

and

$$I_{\kappa,\iota} = \int_{\Im_\kappa}^{\Im_{\kappa+1}} (\Im - \Im_{\kappa})(\Im_{\jmath+1} - \Im)^{\iota-1} d\Im.$$

We proceed by evaluating and reducing the integrals $I_{\kappa-1,\iota}$ and $I_{\kappa,\iota}$, yielding:

$$\begin{aligned} I_{-1+\kappa,\iota} &= -\frac{1}{\iota}\Big[(-\Im_{-1+\kappa} + \Im_{\kappa+1})(\Im_{\jmath+1} - \Im_{\kappa+1})^{\iota} - (-\Im_{-1+\kappa} + \Im_{\kappa})(-\Im_{\kappa} + \Im_{\jmath+1})^{\iota}\Big] \\ &\quad -\frac{1}{\iota(-1+\iota)}\Big[(-\Im_{1+\kappa} + \Im_{\jmath+1})^{\iota+1} - (-\Im_{\kappa} + \Im_{\jmath+1})^{1+\iota}\Big], \\ I_{\kappa,\iota} &= -\frac{1}{\iota}\Big[(\Im_{1+\kappa} - \Im_{\kappa})(\Im_{1+\jmath} - \Im_{1+\kappa})^{\wp}\Big] \\ &\quad -\frac{1}{\iota(-1+\iota)}\Big[(-\Im_{1+\kappa} + \Im_{1+\jmath})^{1+\iota} - (-\Im_{\kappa} + \Im_{1+\jmath})^{1+\iota}\Big]. \end{aligned}$$

Assigning $\Im_\varkappa = i\hbar$, the following result is straightforwardly obtained: By setting $\Im_\varkappa = i\hbar$, one can easily deduce:

$$\begin{aligned} I_{\kappa-1,\iota} &= -\frac{\hbar^{\iota+1}}{\iota(\iota+1)}\Big[(-\kappa+\jmath+1)^{\iota}(-\kappa+\jmath+2+\iota) \\ &\quad -(-\kappa+\jmath)^{\iota}(-\kappa+2\iota+\jmath+2)\Big], \end{aligned} \tag{5.6}$$

and

$$I_{\kappa,\iota} = \frac{\hbar^{\iota+1}}{\iota(\iota+1)}\Big[(\jmath+1-\kappa)^{\iota+1} - (\jmath-\kappa)^{\iota}(\iota+1+\jmath-\kappa)\Big]. \tag{5.7}$$

By substituting Eqs (5.6) and (5.7) into Eq (5.5), we obtain:

$$\begin{aligned} S(\Im_{\jmath+1}) = S(\Im_0) + \frac{(1-\iota)}{\mathbb{N}(\iota)}[\mathbb{K}_1(S(\Im_\jmath), \Im_\jmath)] + \frac{\iota}{\mathbb{N}(\iota)}\sum_{\kappa=0}^{\jmath}\Big(\frac{\mathbb{K}_1(S(\Im_\jmath), \Im_\jmath)}{\iota(\iota+2)} \\ \times \hbar^{\iota}\Big[(-\kappa+\jmath+1)^{\iota}(\jmath-\kappa+\iota+2) - (\jmath-\kappa)^{\iota}(-\kappa+\jmath+2+2\iota)\Big] \\ - \frac{\mathbb{K}_1(S(\Im_{-1+\jmath}), \Im_{-1+\jmath})}{\iota(\iota+2)}\hbar^{\wp} \times \Big[(-\kappa+1+\jmath)^{1+\iota} - (-\kappa+\jmath)^{\iota}(\jmath-\kappa+1+\iota)\Big]\Big), \end{aligned} \tag{5.8}$$

$$
\begin{aligned}
I(\mathfrak{I}_{J+1}) &= I(\mathfrak{I}_0) + \frac{(1-\iota)}{\mathbb{N}(\iota)}[\mathbb{K}_2(I(\mathfrak{I}_J), \mathfrak{I}_J)] + \frac{\iota}{\mathbb{N}(\iota)} \sum_{\kappa=0}^{J} \Big(\frac{\mathbb{K}_2(I(\mathfrak{I}_J), \mathfrak{I}_J)}{\iota(\iota+2)} \\
&\times \hbar^{\iota} \Big[(-\kappa + J + 1)^{\iota} (J - \kappa + \iota + 2) - (J-\kappa)^{\iota} (-\kappa + J + 2 + 2\iota) \Big] \\
&- \frac{\mathbb{K}_2(I(\mathfrak{I}_{J-1}), \mathfrak{I}_{-1+J})}{\iota(\iota+2)} \times \hbar^{\iota} \Big[(-\kappa + 1 + J)^{1+\iota} - (-\kappa + J)^{\iota} (J - \kappa + 1 + \iota) \Big] \Big), \qquad (5.9)
\end{aligned}
$$

$$
\begin{aligned}
T(\mathfrak{I}_{J+1}) &= T(\mathfrak{I}_0) + \frac{(1-\iota)}{\mathbb{N}(\iota)}[\mathbb{K}_3(T(\mathfrak{I}_J), \mathfrak{I}_J)] + \frac{\iota}{\mathbb{N}(\iota)} \sum_{\kappa=0}^{J} \Big(\frac{\mathbb{K}_3(T(\mathfrak{I}_J), \mathfrak{I}_J)}{\iota(\iota+2)} \\
&\times \hbar^{\iota} \Big[(-\kappa + J + 1)^{\iota} (J - \kappa + \iota + 2) - (J-\kappa)^{\iota} (-\kappa + J + 2 + 2\iota) \Big] \\
&- \frac{\mathbb{K}_3(T(\mathfrak{I}_{J-1}), \mathfrak{I}_{-1+J})}{\iota(\iota+2)} \hbar^{\iota} \Big[(-\kappa + 1 + J)^{\iota+1} - (-\kappa + J)^{\iota} (J - \kappa + 1 + \iota) \Big] \Big), \qquad (5.10)
\end{aligned}
$$

$$
\begin{aligned}
R(\mathfrak{I}_{J+1}) &= R(\mathfrak{I}_0) + \frac{(1-\iota)}{\mathbb{N}(\iota)}[\mathbb{K}_4(R(\mathfrak{I}_J), \mathfrak{I}_J)] + \frac{\iota}{\mathbb{N}(\iota)} \sum_{\kappa=0}^{J} \Big(\frac{\mathbb{K}_4(R(\mathfrak{I}_J), \mathfrak{I}_J)}{\iota(\iota+2)} \\
&\times \hbar^{\iota} \Big[(-\kappa + J + 1)^{\iota} (J - \kappa + \iota + 2) - (J-\kappa)^{\iota} (-\kappa + J + 2 + 2\iota) \Big] \\
&- \frac{\mathbb{K}_4(R(\mathfrak{I}_{J-1}), \iota_{-1+J})}{\iota(\iota+2)} \hbar^{\iota} \Big[(-\kappa + 1 + J)^{\iota+1} - (-\kappa + J)^{\iota} (J - \kappa + 1 + \iota) \Big] \Big), \qquad (5.11)
\end{aligned}
$$

$$
\begin{aligned}
V(\mathfrak{I}_{J+1}) &= V(\mathfrak{I}_0) + \frac{(1-\iota)}{\mathbb{N}(\iota)}[\mathbb{K}_5(V(\mathfrak{I}_J), \mathfrak{I}_J)] + \frac{\iota}{\mathbb{N}(\iota)} \sum_{\kappa=0}^{J} \Big(\frac{\mathbb{K}_5(V(\mathfrak{I}_J), \mathfrak{I}_J)}{\iota(\iota+2)} \\
&\times \hbar^{\iota} \Big[(-\kappa + J + 1)^{\iota} (J - \kappa + \iota + 2) - (J-\kappa)^{\iota} (-\kappa + J + 2 + 2\iota) \Big] \\
&- \frac{\mathbb{K}_5(V(\mathfrak{I}_{J-1}), \mathfrak{I}_{-1+J})}{\iota(\iota+2)} \hbar^{\iota} \Big[(-\kappa + 1 + J)^{\iota+1} - (-\kappa + J)^{\iota} (J - \kappa + 1 + \iota) \Big] \Big), \qquad (5.12)
\end{aligned}
$$

$$
\begin{aligned}
W(\mathfrak{I}_{J+1}) &= W(\mathfrak{I}_0) + \frac{(1-\iota)}{\mathbb{N}(\iota)}[\mathbb{K}_6(W(\mathfrak{I}_J), \mathfrak{I}_J)] + \frac{\iota}{\mathbb{N}(\iota)} \sum_{\kappa=0}^{J} \Big(\frac{\mathbb{K}_6(W(\mathfrak{I}_J), \mathfrak{I}_J)}{\iota(\iota+2)} \\
&\times \hbar^{\iota} \Big[(-\kappa + J + 1)^{\iota} (J - \kappa + \iota + 2) - (J-\kappa)^{\iota} (-\kappa + J + 2 + 2\iota) \Big] \\
&- \frac{\mathbb{K}_6(W(\mathfrak{I}_{J-1}), \mathfrak{I}_{-1+J})}{\iota(\iota+2)} \hbar^{\iota} \Big[(-\kappa + 1 + J)^{\iota+1} - (-\kappa + J)^{\iota} (J - \kappa + 1 + \iota) \Big] \Big). \qquad (5.13)
\end{aligned}
$$

6. Numerical simulation and discussion

In this section, an approximate solution to model (2.1) is obtained by utilizing various parameter sets provided in Table 1, to assess the performance of the proposed numerical method.

Table 1. Parameter values employed in model (2.1) under various control scenarios.

Parameter	Value	Parameter	value	Parameter	Value	Parameter	Value
$S(0)$	100	I(0)	30	T(0)	25	ν	5
$R(0)$	10	V(0)	600	W(0)	100	β	0.001
ϵ_1	0.001	β_1	0.00001	β_2	0.0012	γ	0.04
α	0.75	ϵ_2	0.002	μ_1	0.00039	b_1	20
μ_2	0.1	δ_1	0.01	δ_2	0.21	b_2	100
ηI	0.01	β_3	0.001				

We simulate the outcomes of the preceding algorithms for the different categories in (27)–(32) using Matlab and the parameter values from Table 1, as shown in Figures 2–7.

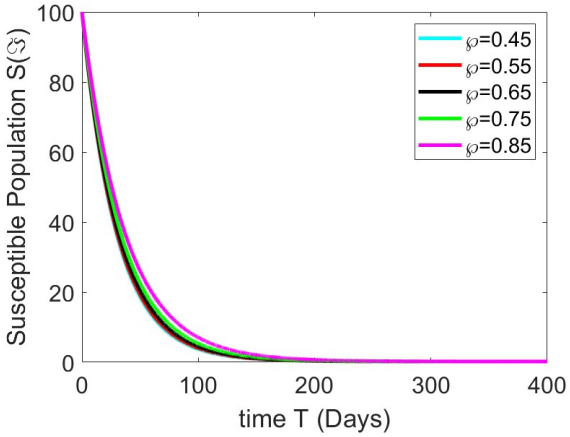

Figure 2. Numerical simulation results illustrating the dynamics of the susceptible population.

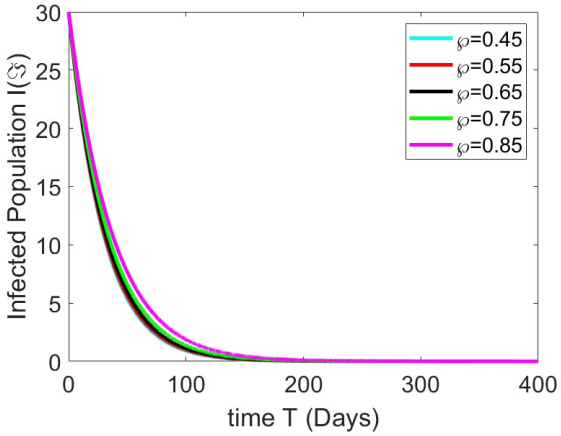

Figure 3. Numerical simulation results illustrating the dynamics of infectious population.

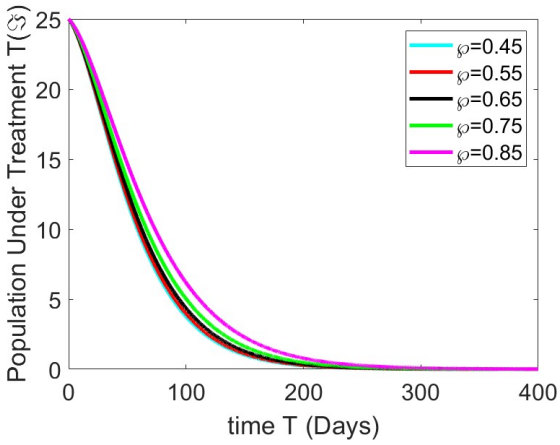

Figure 4. Numerical simulation results illustrating the dynamics of the population under treatment.

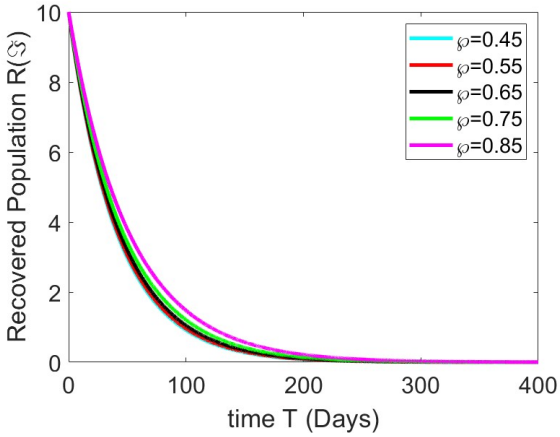

Figure 5. Numerical simulation results illustrating the dynamics of recovered population.

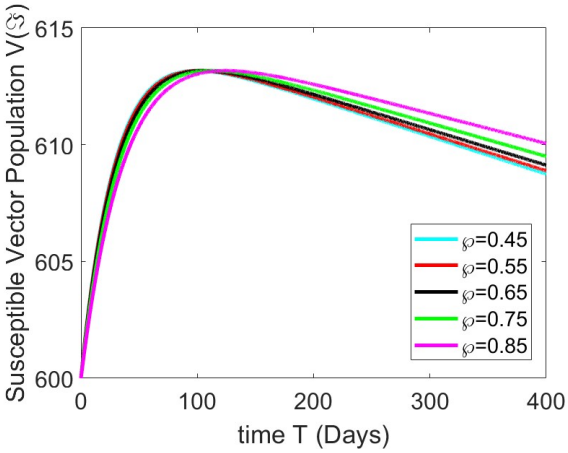

Figure 6. Numerical simulation results illustrating the dynamics of the susceptible vector population.

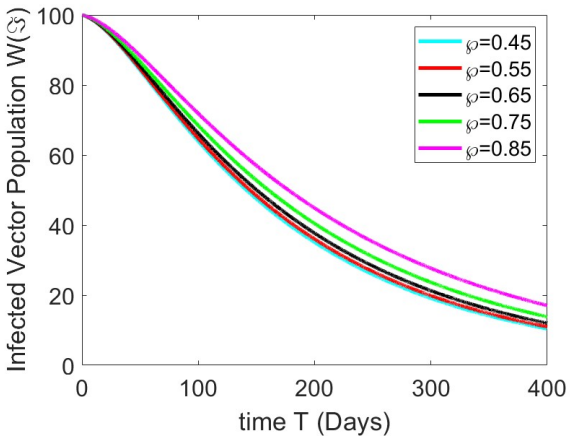

Figure 7. Numerical simulation results illustrating the dynamics of the infected vector population.

The dataset is divided into three segments: 70% for training, 15% for testing, and 15% for validation. Each segment is analyzed under a distinct fractional-order setting. To enhance the mathematical rigor of our methodology, we formally define the neural network mapping as $\mathcal{F} : X \to Y$, where X represents the input space (e.g., time points) and Y denotes the approximated solution values of the compartmental model. The network minimizes the mean squared error (MSE), defined as:

$$\text{MSE} = \frac{1}{n}\sum_{i=1}^{n}(y_i - \hat{y}_i)^2,$$

where y_i are the reference solutions obtained via the fractional Adams-Bashforth method and $\hat{y}_i$ are the corresponding ANN predictions. The feedforward neural network architecture includes one input layer, two hidden layers with 10 neurons each, and one output layer. Sigmoid activation functions are used in the hidden layers, while a linear activation function is applied at the output. Training is performed using the Levenberg-Marquardt algorithm with backpropagation until convergence based on MSE minimization.

The ANN serves solely as a solution approximator, aiming to reproduce the numerical behavior of the fractional-order model across time. It is not used for parameter estimation or data-driven prediction from real-world datasets. Rather, it is trained on simulation-generated data to verify the smoothness, consistency, and robustness of the numerical scheme. The theoretical justification for using an ANN lies in the universal approximation theorem, which states that a feedforward neural network with at least one hidden layer can approximate any continuous function on a compact domain, provided there are sufficient neurons and appropriate activation functions. This supports our use of ANN to approximate the underlying solution operator. A schematic diagram has been included to illustrate how the network maps input-output pairs and captures the compartmental dynamics, thereby offering insight into the long-term behavior patterns of the system.

The implementation of the artificial neural network (ANN) utilizing the Adam-Bashforth method is illustrated in Figure 8(a). Figure 8(b) illustrates the model's performance at the 1000 epoch, where a mean square error of approximately 3.8534e-12 was achieved. The training progression is shown in Figure 8(c), while Figure 8(d) presents the error histogram, indicating a minimum value of $3.5e-07$ as

the most accurate outcome observed in this experiment. Figure 8(e) demonstrates both the prediction errors and the best fit for the training and testing datasets. Additionally, Figure 9 displays the regression analysis applied to the complete dataset, which includes both the training and testing sets. The close alignment of the data points with the regression line confirms the model's strong training performance. The coefficient of determination R is approximately equal to 1.

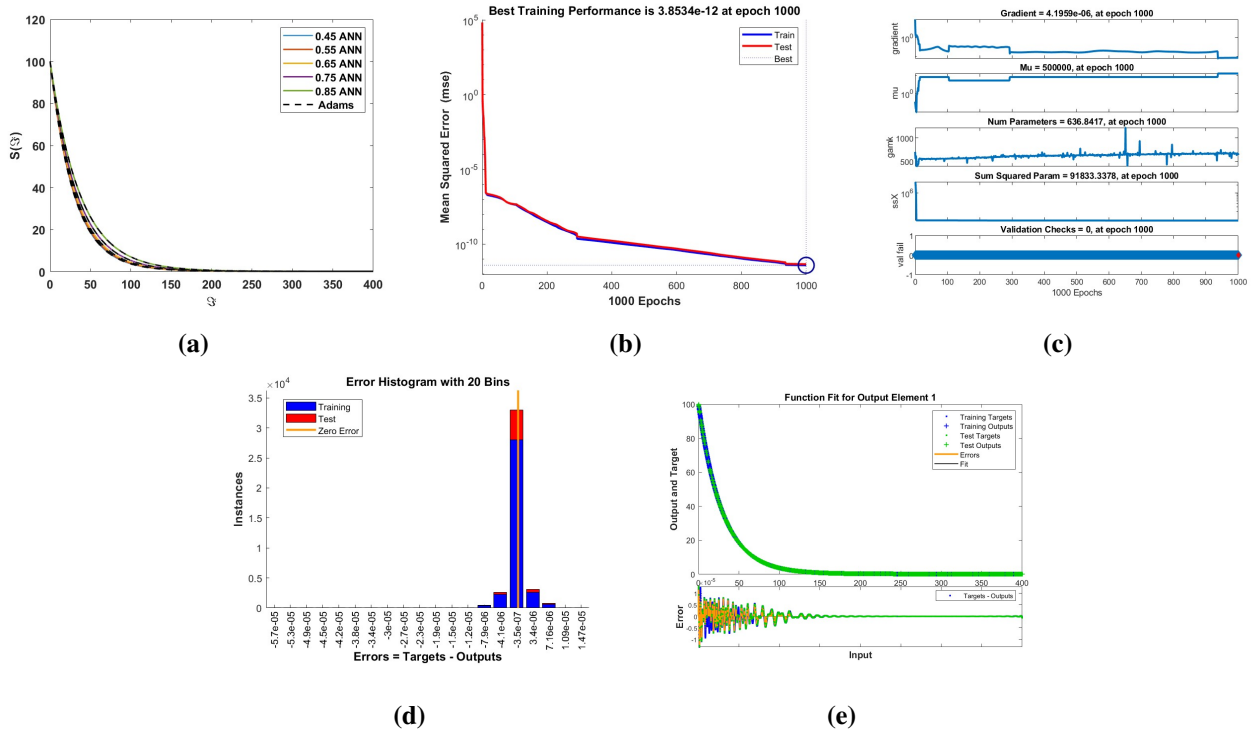

Figure 8. Statistical performance of the proposed model is illustrated through: (a) comparative analysis, (b) mean squared error, (c) regression outcomes, (d) error distribution histogram, and (e) ANN training performance.

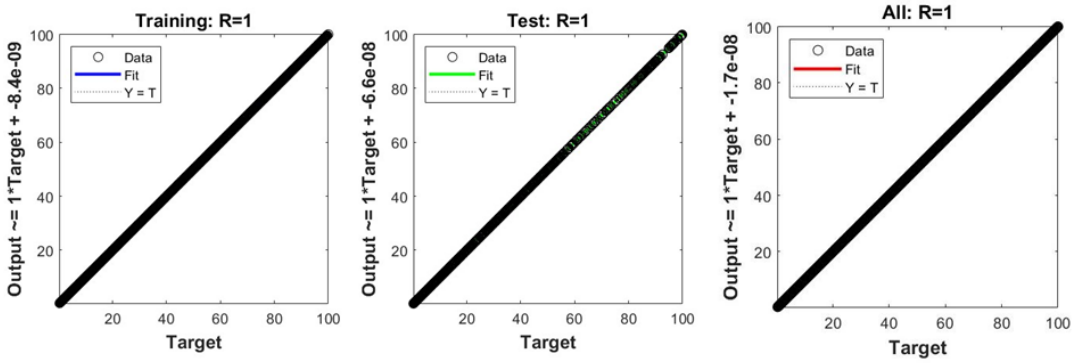

Figure 9. Dynamic visualization of regression results using ANNs applied to the proposed system.

The integration of ANN with the Adam-Bashforth method is illustrated in Figure 10(a). Figure 10(b) presents the model's performance at the 546 epoch, with a reported mean square error

of 1.1815e-11. Training progression is displayed in Figure 10(c,d). The error distribution is shown in Figure 10(e), where the minimum value recorded in this experiment is -9.8e-07. Figure 10(e) also illustrates the best alignment between the model predictions and the actual values for both training and testing datasets, along with their respective errors. The regression outcomes for the training, testing, and overall data are summarized in Figure 11. The concentration of data points along the regression line confirms that the ANN was trained successfully. The correlation coefficient R obtained is approximately 1.

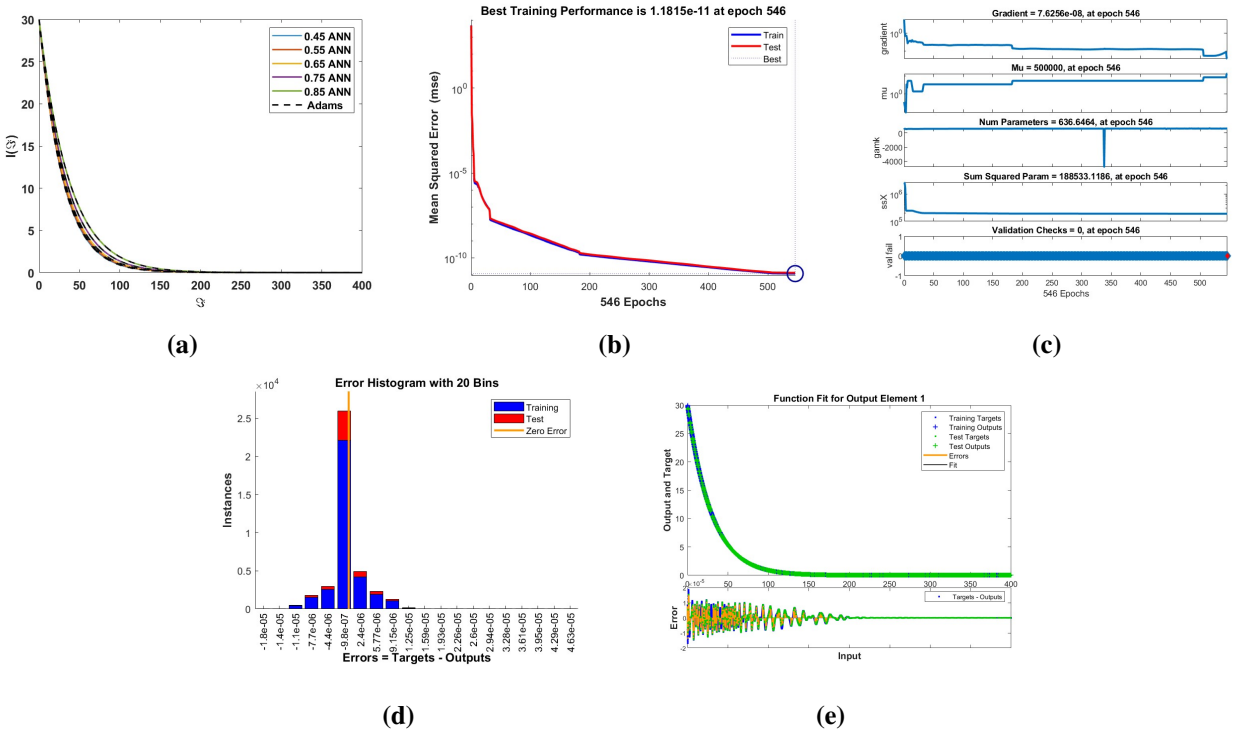

Figure 10. Statistical performance of the proposed model is illustrated through: (a) comparative analysis, (b) mean squared error, (c) regression outcomes, (d) error distribution histogram, and (e) ANN training performance.

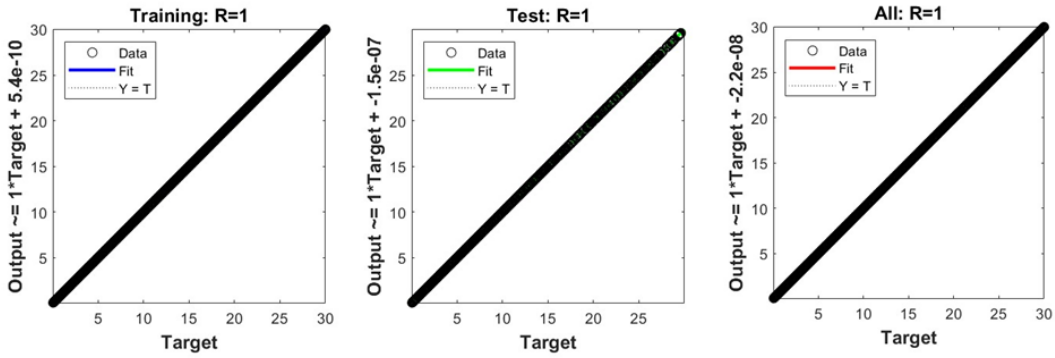

Figure 11. Dynamic visualization of regression results using ANNs applied to the proposed system.

The utilization of ANN combined with the Adam-Bashforth technique is illustrated in Figure 12(a). Figure 12(b) presents the model's accuracy at epoch 772, yielding a mean square error of approximately 6.4375e-12. The progression of the training phase is depicted in Figure 12(c,d). The error histogram, shown in Figure 12(d), reveals a minimum error value of 3.87e-07. Figure 12(e) demonstrates the best fit between the predicted and actual data for both training and testing, alongside their corresponding errors. Additionally, the regression analysis for the complete dataset is presented in Figure 13. The precise alignment of the data points along the regression line indicates that the neural network was trained effectively. The resulting correlation coefficient R is approximately equal to 1.

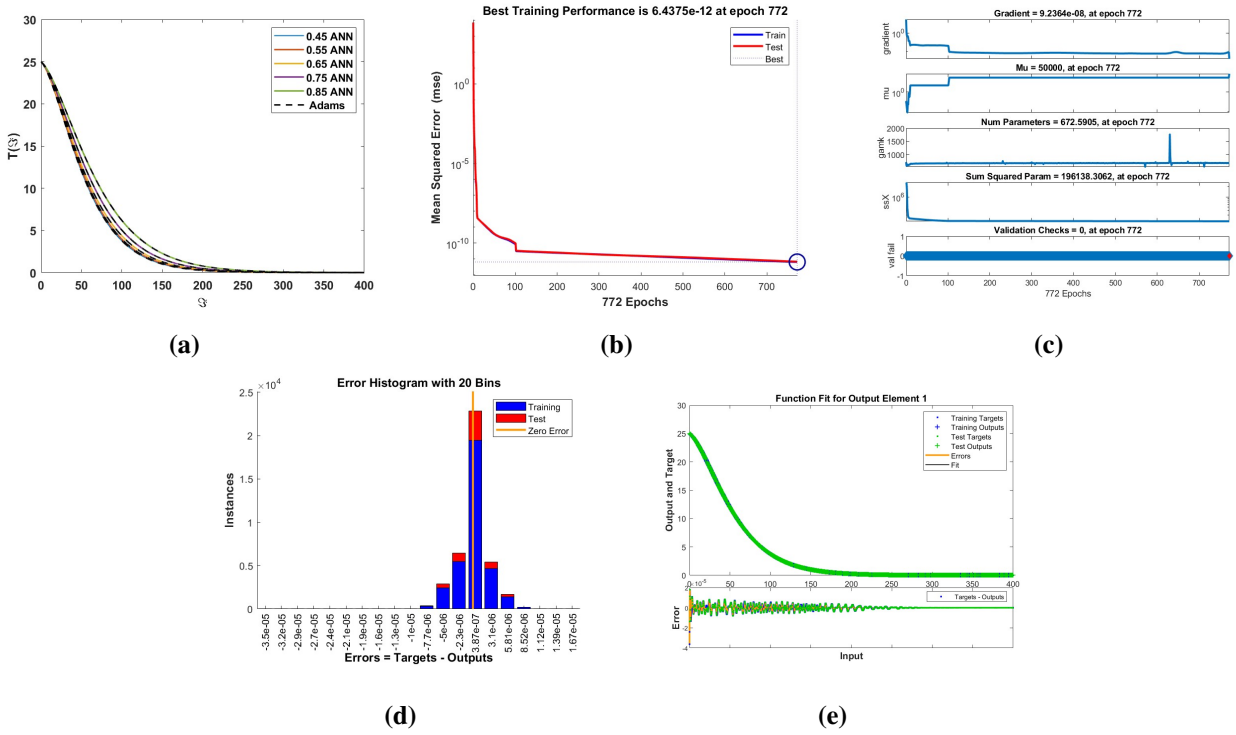

Figure 12. Statistical performance of the proposed model is illustrated through: (a) comparative analysis, (b) mean squared error, (c) regression outcomes, (d) error distribution histogram, and (e) ANN training performance.

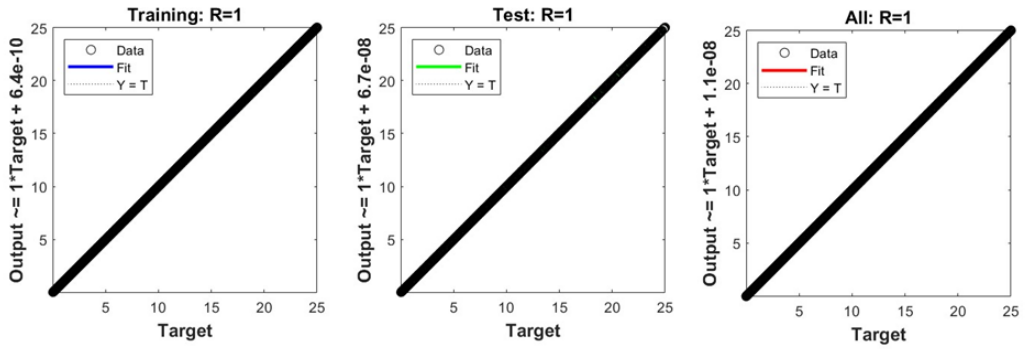

Figure 13. Dynamic visualization of regression results using ANNs applied to the proposed system.

The application of ANN in conjunction with the Adam-Bashforth method is demonstrated in Figure 14(a). Figure 14(b) illustrates the model's performance at the 547 epoch, yielding a mean square error of approximately 1.2134e-12. The training dynamics are presented in Figure 14(c), while the error distribution is depicted in Figure 14(d), where the minimum error recorded is 2.68e-07. Figure 14(e) shows the best alignment between predicted and actual data for both training and testing sets, along with corresponding error measurements. The regression analysis covering all phases-training, and testing-is displayed in Figure 15. The precise alignment of data points along the regression line confirms that the ANN has been trained effectively. The correlation coefficient R obtained is approximately 1.

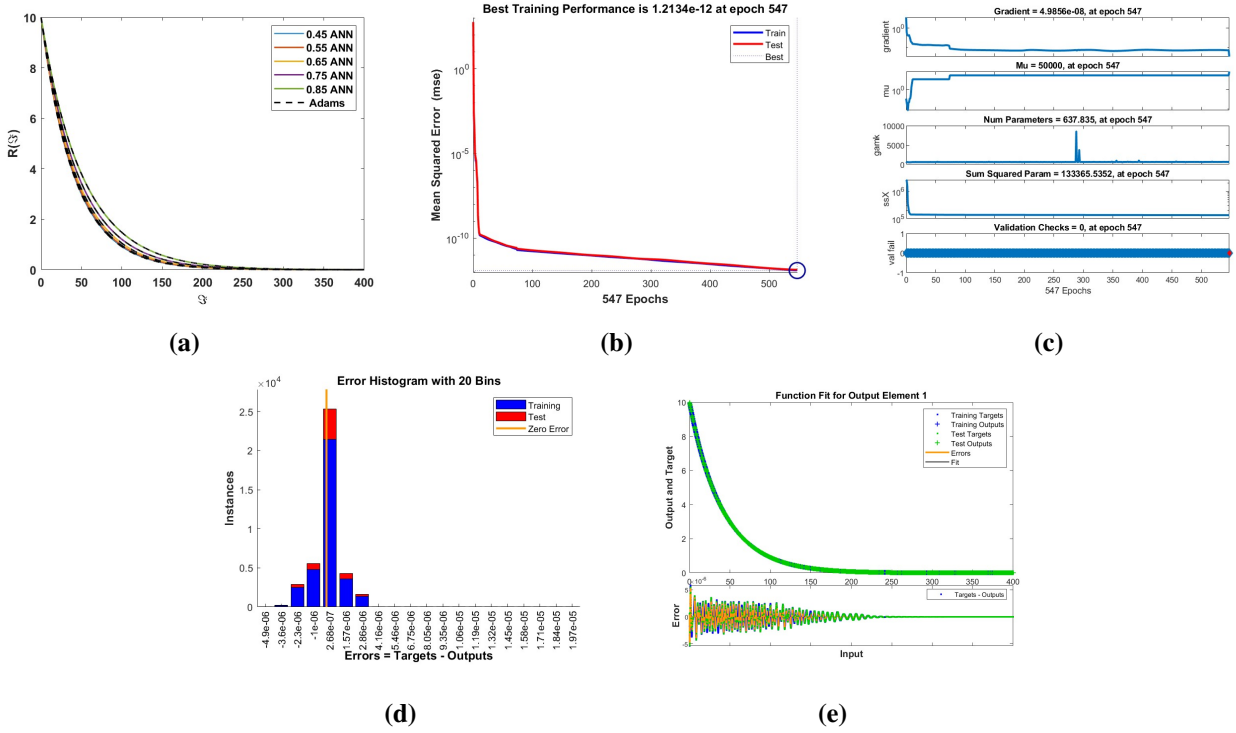

Figure 14. Statistical performance of the proposed model is illustrated through: (a) comparative analysis, (b) mean squared error, (c) regression outcomes, (d) error distribution histogram, and (e) ANN training performance.

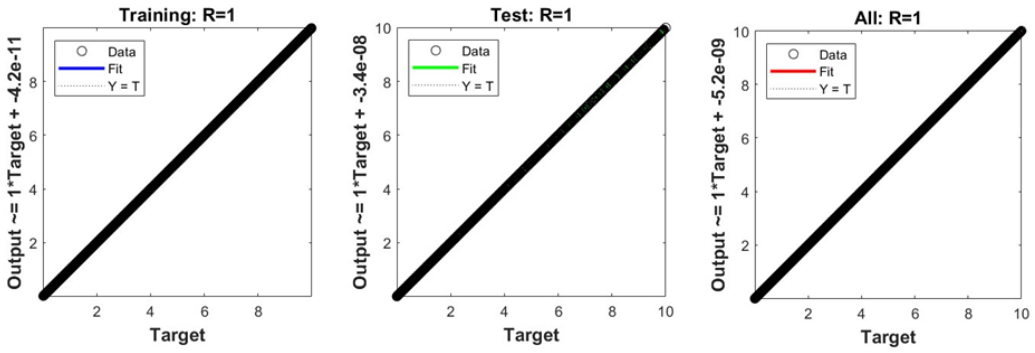

Figure 15. Dynamic visualization of regression results using ANNs applied to the proposed system.

The implementation of the ANN in conjunction with the Adam-Bashforth numerical scheme is illustrated in Figure 16(a). The model's effectiveness at the 1000th epoch is illustrated in Figure 16(b), where it achieves a mean square error of approximately 4.4469e-12. The progression of the training phase is visualized in Figure 16(c), while the error distribution is presented in Figure 16(d), indicating a minimum value of -1.6e-06. Figure 16(e) demonstrates both the prediction errors and the optimal fit between training and testing datasets. Regression analysis for the complete dataset, including training, testing, and validation, is provided in Figure 17. The consistency between predicted and actual values confirms that the model was trained effectively. The data alignment along the regression line further supports this. The resulting correlation coefficient R is approximately 1.

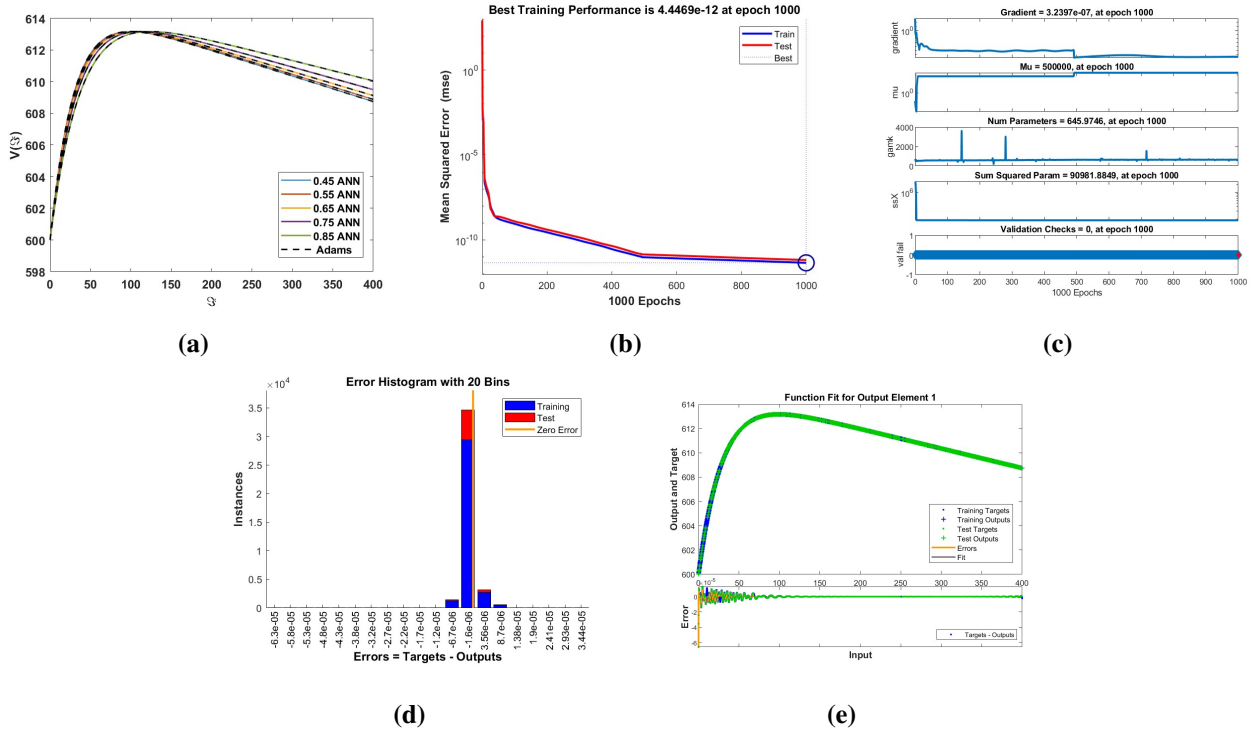

Figure 16. Statistical performance of the proposed model is illustrated through: (a) comparative analysis, (b) mean squared error, (c) regression outcomes, (d) error distribution histogram, and (e) ANN training performance.

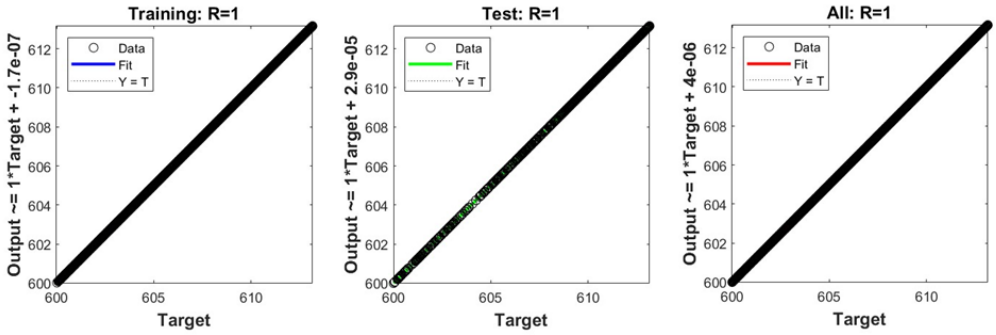

Figure 17. Dynamic visualization of regression results using ANNs applied to the proposed system.

The ANN implementation, coupled with the Adam-Bashforth scheme, is illustrated in Figure 18(a). Figure 18(b) demonstrates the model's performance at the 1000 epoch, achieving a mean squared error of approximately 9.6134e-10. The progression of the training process is shown in Figure 18(c). Figure 18(d) presents the error histogram, where the optimal result attained is -4e-06. As depicted in Figure 18(e), both training and testing datasets exhibit a strong fit. Figure 19 provides the regression plots for the training, testing, and overall dataset. These visualizations confirm that the ANN was effectively trained, as the data aligns closely with the regression line. The computed correlation coefficient R is approximately equal to 1.

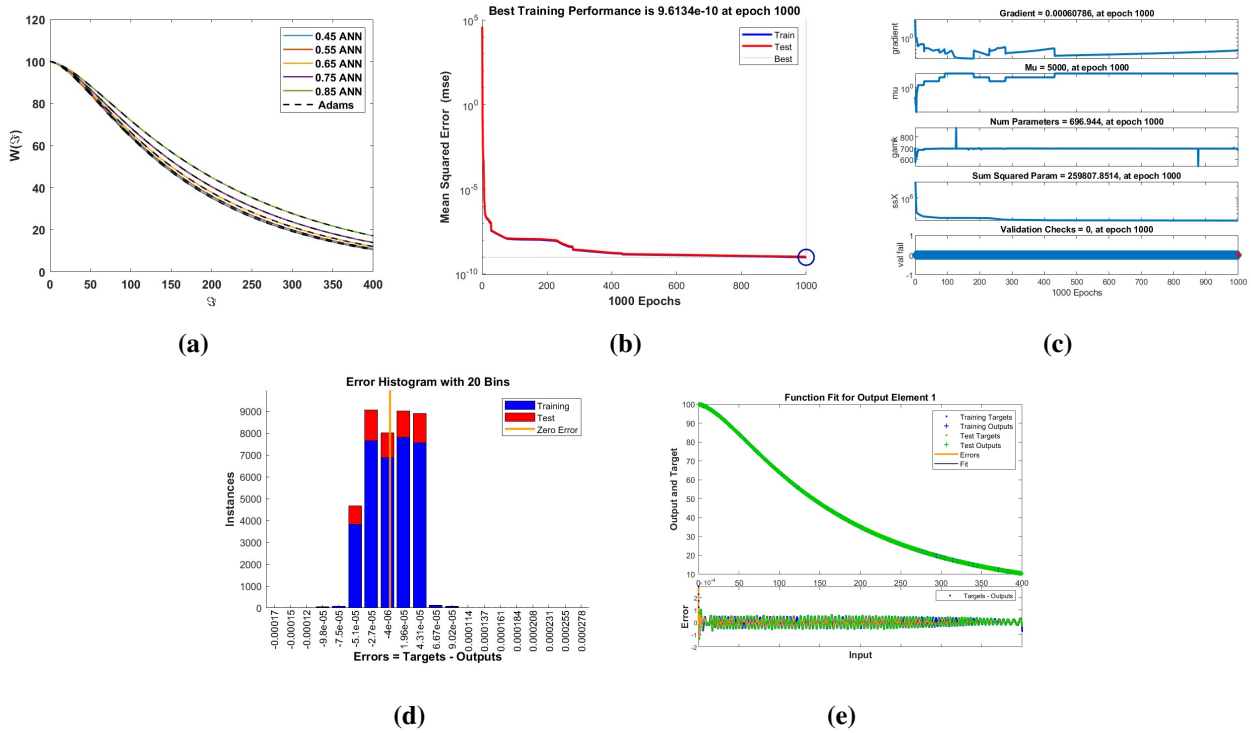

Figure 18. Statistical performance of the proposed model is illustrated through: (a) comparative analysis, (b) mean squared error, (c) regression outcomes, (d) error distribution histogram, and (e) ANN training performance.

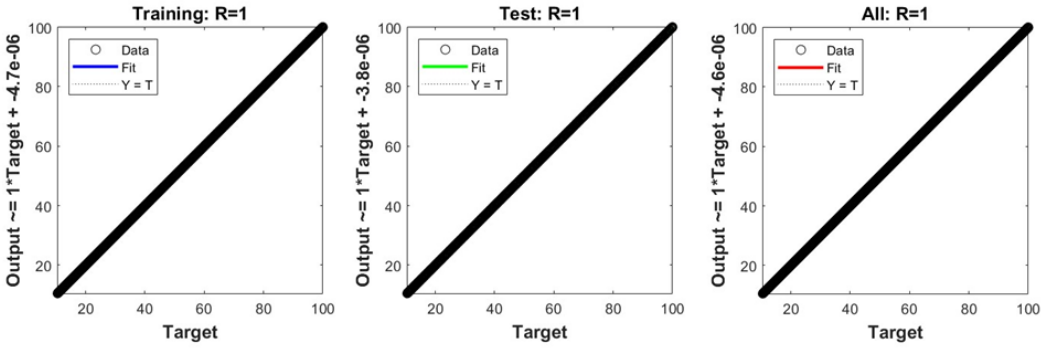

Figure 19. Dynamic visualization of regression results using ANNs applied to the proposed system.

7. Conclusions

In this study, we analyzed a fractional-order mathematical model for the transmission dynamics of vector-borne diseases formulated under the ABC operator. The existence of solutions was established through fixed point theory, and the Adams-Bashforth scheme was employed to obtain approximate numerical solutions. Stability analysis was carried out using Ulam-Hyers-type techniques from nonlinear theory.

To support the theoretical results, numerical experiments were conducted for two distinct scenarios, with and without intervention strategies. The simulations demonstrated that all compartments of the model achieved stability and convergence. It was observed that for small fractional orders, the decay process stabilizes rapidly, while for higher orders, the growth process reaches stability more efficiently.

The fractional model provides broader insights by incorporating memory and hereditary characteristics, which are absent in classical integer-order frameworks. Consequently, model (2) outperforms its integer-order counterpart, model (1), by capturing richer dynamic behavior. Using ANN techniques applied to a vector-borne disease model, the dataset is partitioned into training, testing, and validation subsets, with an in-depth analysis carried out for each. This study enhances the application of the ABC derivative by offering more profound insights into the dynamics of crossover behavior. One of the key findings from the simulation results indicates that higher vaccine efficacy is closely associated with improved recovery outcomes. Through the examination of extensive numerical and graphical data, meaningful patterns and relationships were uncovered. Future investigations may consider incorporating more generalized nonlocal operators to enhance modeling capabilities further and explore new biological insights.

Use of Generative-AI tools declaration

The author declares he has not used Artificial Intelligence (AI) tools in the creation of this article.

Acknowledgment

The author express his sincere appreciation to Taif University, Saudi Arabia, for the support it has offer under project number (TU-DSPP-2024-259).

Conflict of interest

The author declares no conflict of interest in this paper.

References

1. M. W. Service, *Blood-sucking insects: vectors of disease*, London: Edward Arnold, 1986.
2. Q. Hou, Z. Jin, S. Ruan, Dynamics of rabies epidemics and the impact of control efforts in Guangdong Province, China, *J. Theoret. Biol.*, **300** (2012), 39–47. https://doi.org/10.1016/j.jtbi.2012.01.006

3. R. M. Anderson, H. C. Jackson, R. M. May, A. M. Smith, Population dynamics of fox rabies in Europe, *Nature*, **289** (1981), 765–771. https://doi.org/10.1038/289765a0
4. D. L. Smith, B. Lucey, L. A. Waller, J. E. Childs, L. A. Real, Predicting the spatial dynamics of rabies epidemics on heterogeneous landscapes, *Proc. National Acad. Sci.*, **99** (2002), 3668–3672. https://doi.org/10.1073/pnas.042400799
5. C. A. Russell, D. L. Smith, J. E. Childs, L. A. Real, Predictive spatial dynamics and strategic planning for raccoon rabies emergence in Ohio, *PLoS Biol.*, **3** (2005), e88. https://doi.org/10.1371/journal.pbio.0030088
6. E. Asano, L. J. Gross, S. Lenhart, L. A. Real, Optimal control of vaccine distribution in a rabies metapopulation model, *Math. Biosci. Eng.*, **5** (2008), 219–238. https://doi.org/10.3934/mbe.2008.5.219
7. M. Goyal, H. M. Baskonus, A. Prakash, An efficient technique for a time fractional model of lassa hemorrhagic fever spreading in pregnant women, *Eur. Phys. J. Plus*, **134** (2019), 482. https://doi.org/10.1140/epjp/i2019-12854-0
8. W. Gao, P. Veeresha, D. G. Prakasha, H. M. Baskonus, G. Yel, New approach for the model describing the deathly disease in pregnant women using Mittag-Leffler function, *Chaos Solitons Fract.*, **134** (2020), 109696. https://doi.org/10.1016/j.chaos.2020.109696
9. J. Zhang, Z. Jin, G. Q. Sun, T. Zhou, S. Ruan, Analysis of rabies in China: transmission dynamics and control, *PLoS One*, **6** (2011), e20891. https://doi.org/10.1371/journal.pone.0020891
10. M. Farman, A. Akgül, A. Ahmad, D. Baleanu, M. U. Saleem, Dynamical transmission of coronavirus model with analysis and simulation, *Comput. Model. Eng. Sci.*, **127** (2021), 753–769. https://doi.org/10.32604/cmes.2021.014882
11. M. Javidi, B. Ahmad, A study of a fractional-order cholera model, *Appl. Math. Inform. Sci.*, **8** (2014), 2195. https://doi.org/10.12785/amis/080513
12. V. S. Ertürk, G. Zaman, S. Momani, A numeric-analytic method for approximating a giving up smoking model containing fractional derivatives, *Comput. Math. Appl.*, **64** (2012), 3065–3074. https://doi.org/10.1016/j.camwa.2012.02.002
13. J. Singh, D. Kumar, M. A. Qurashi, D. Baleanu, A new fractional model for giving up smoking dynamics, *Adv. Differ. Equ.*, **2017** (2017), 88. https://doi.org/10.1186/s13662-017-1139-9
14. K. Abuasbeh, R. Shafqat, A. Alsinai, M. Awadalla, Analysis of the mathematical modelling of COVID-19 by using mild solution with delay Caputo operator, *Symmetry*, **15** (2023), 286. https://doi.org/10.3390/sym15020286
15. A. Moumen, R. Shafqat, A. Alsinai, H. Boulares, M. Cancan, M. B. Jeelani, Analysis of fractional stochastic evolution equations by using Hilfer derivative of finite approximate controllability, *AIMS Math.*, **8** (2023), 16094–16114. https://doi.org/10.3934/math.2023821
16. H. Khan, Y. Li, A. Khan, A. Khan, Existence of solution for a fractional-order Lotka-Volterra reaction-diffusion model with Mittag-Leffler kernel, *Math. Meth. Appl. Sci.*, **42** (2019), 3377–3387. https://doi.org/10.1002/mma.5590
17. R. A. Khan, K. Shah, Existence and uniqueness of solutions to fractional order multi-point boundary value problems, *Commun. Appl. Anal.*, **19** (2015), 515–525.

18. T. Khan, F. A. Rihan, Q. M. Al-Mdallal, An epidemiological model for analysing pandemic trends of novel coronavirus transmission with optimal control, *J. Biol. Dyn.*, **18** (2024), 2299001. https://doi.org/10.1080/17513758.2023.2299001

19. T. Khan, Z. S. Qian, R. Ullah, B. A. Alwan, G. Zaman, Q. M. Al-Mdallal, et al., The transmission dynamics of hepatitis B virus via the fractional-order epidemiological model, *Complexity*, **2021**, (2021), 8752161. https://doi.org/10.1155/2021/8752161

20. D. Baleanu, A. Fernandez, A. Akgül, On a fractional operator combining proportional and classical differintegrals, *Mathematics*, **8** (2020), 360. https://doi.org/10.3390/math8030360

21. M. Caputo, M. Fabrizio, A new definition of fractional derivative without singular kernel, *Progr. Fract. Differ. Appl.*, **1** (2015), 73–85. https://doi.org/10.12785/pfda/010201

22. A. Atangana, D. Baleanu, New fractional derivatives with nonlocal and non-singular kernel: theory and application to heat transfer model, preprint paper, 2016. https://doi.org/10.48550/arXiv.1602.03408

23. A. Turab, R. Shafqat, S. Muhammad, M. Shuaib, M. F. Khan, M. Kamal, Predictive modeling of hepatitis B viral dynamics: a caputo derivative-based approach using artificial neural networks, *Sci. Rep.*, **14** (2024), 21853. https://doi.org/10.1038/s41598-024-70788-7

24. H. Liu, M. Liu, D. Li, W. Zheng, L. Yin, R. Wang, Recent advances in pulse-coupled neural networks with applications in image processing, *Electronics*, **11** (2022), 3264. https://doi.org/10.3390/electronics11203264

25. R. Shafqat, A. Alsaadi, Artificial neural networks for stability analysis and simulation of delayed rabies spread models, *AIMS Math.*, **9** (2024), 33495–33531. https://doi.org/10.3934/math.20241599

AIMS Press